High precision 5 MeV Mott polarimeter

J. M. Grames,[1] C. K. Sinclair,[1,*] M. Poelker,[1] X. Roca-Maza,[2] M. L. Stutzman,[1] R. Suleiman,[1] Md. A. Mamun,[1,3] M. McHugh,[4,†] D. Moser,[1] J. Hansknecht,[1] B. Moffit,[1] and T. J. Gay[5]

[1]*Thomas Jefferson National Accelerator Facility, Newport News, Virginia 23606, USA*

[2]*Departimento di Fisica, Universita degli Studi di Milano, and Istituto Nazionale di Fisica Nucleare, Sezione di Milano, Milano 20133, Italy*

[3]*Department of Mechanical and Aerospace Engineering, Old Dominion University, Norfolk, Virginia 23529, USA*

[4]*Physics Department, George Washington University, Washington, DC 20052, USA*

[5]*Jorgensen Hall, University of Nebraska, Lincoln, Nebraska 68588, USA*

(Received 13 February 2020; accepted 27 April 2020; published xxxxxxxxx)

We report on the design and performance of a Mott polarimeter optimized for a nominal 5-MeV electron beam from the Continuous Electron Beam Accelerator Facility (CEBAF) injector. The rf time structure of this beam allows the use of time of flight in the scattered electron detection, making it possible to cleanly isolate those detected electrons that originate from the scattering foil, and resulting in measured scattering asymmetries which are exceptionally stable over a broad range of beam conditions, beam currents, and foil thicknesses. In two separate series of measurements from two different photocathode electron sources, we have measured the Mott scattering asymmetries produced by an approximately 86% transversely polarized electron beam incident on ten gold foils with nominal thicknesses between 50 and 1000 nm. The statistical uncertainty of the measured asymmetry from each foil is below 0.25%. Within this statistical precision, the measured asymmetry was unaffected by ± 1-mm shifts in the beam position on the target foil, and by beam current changes and dead-time effects over a wide range of beam currents. The overall uncertainty of our beam polarization measurement, arising from the uncertainty in the value of the scattering asymmetry at zero foil thickness as determined from our fits to the measured asymmetries versus scattering foil thicknesses, the estimated systematic effects, and the (dominant) uncertainty from the calculation of the theoretical Sherman function, is 0.61%. A simulation of the polarimeter using GEANT4 has confirmed that double scattering in the target foil is the sole source of the dependence of the measured asymmetry on foil thickness, and gives a result for the asymmetry versus foil thickness in good agreement with both our measurements and a simple calculation. Future measurements at different beam energies and with target foils of different atomic numbers will seek to bound uncertainties from small effects such as radiative corrections to the calculation of the polarimeter analyzing power. A simultaneous high-precision measurement of the beam polarization with a different polarimeter, AESOP (Accurate Electron Spin Optical Polarimeter), under development at the University of Nebraska, clearly possible at the CEBAF accelerator, will allow a high-precision comparison of our measured asymmetries with theoretical calculations of the Mott analyzing power. Finally, the improved precision of the current Mott polarimeter along with similar improvements to other Jefferson Lab polarimeters warrants another precision comparison of all of these polarimeters when measuring a beam of the same polarization.

DOI: 10.1103/PhysRevC.00.005500

I. INTRODUCTION

Soon after the publication of Dirac's revolutionary equation for the electron, Mott calculated the elastic scattering of electrons by the Coulomb field of the nucleus in this new formalism [1]. His motivation was to determine whether the anticipated polarization of the scattered electron, produced by spin-orbit coupling and in principle measurable in a double-scattering experiment, could be used to determine the magnetic moment of the free electron. At that time, the then unusual g factor of 2 for the electron was both inferred from measurements of the fine structure of atomic spectra and predicted by Dirac's equation. It was understood at the time that the uncertainty principle precluded the separation of free-electron spins with static electromagnetic fields, and thus a direct measurement of the electron magnetic moment.

Mott's solutions for the spin-flip and non-spin-flip scattering amplitudes are conditionally convergent series in which pairs of terms very nearly cancel, requiring the calculation of many terms to obtain reasonably precise values for the scattering cross section and scattered beam polarization. Although various mathematical transformations were employed to reduce the complexity of the calculations, they remained tedious (see Ref. [2] and references therein). Before the advent of digital computers, calculated values for the cross section and polarization were restricted to a limited number of elec-

*Present address: P.O. Box 8713, Medford, OR, 97501.

†m.j.mchughiii@gmail.com

tron energies and a 90° scattering angle. The first extensive computer calculations of the cross section were published in 1956 by Doggett and Spencer [3], and by Sherman [4], who also calculated the scattered beam polarization, which is transverse to the plane of scattering. Since that time, the analyzing power of Mott scattering has been known as the Sherman function.

Several early attempts to demonstrate electron polarization in a double-scattering experiment gave negative or inconclusive results prior to the first successful measurement by Shull *et al.* [5]. As Mott scattering was the only demonstrated method for producing polarized electrons at the time, experiments using them were uncommon. One early application was a measurement of the free-electron g factor with 0.5% precision, satisfying Mott's original motivation (though not in the way he envisioned) [6]. Following the experimental demonstrations of parity violation in the weak interactions in 1957, Mott polarimeters, coupled with electrostatic spin rotators, were developed in a number of laboratories to measure the longitudinal polarization of beta decay electrons. This led to a much-improved understanding of the experimental technique, and to several well-designed polarimeters [7–9]. The development of polarized electron sources began in the late 1950s, and required polarimetry to quantify and improve their performance [10,11]. Mott scattering at modest energies was universally employed for these studies. All of these early Mott polarimeters operated at energies well below 1 MeV. The experimental challenges, and the problems in computing the effective Sherman function at these relatively low energies, are decidedly different than those encountered at few-MeV energies, and will not be discussed here.

Mott polarimetry at energies well above 1 MeV was first employed in a search for possible time-reversal violation in the beta decay of ^{8}Li [12,13]. The success of this experiment led some of its participants, with collaborators at the Mainz Microtron (MAMI) accelerator at Mainz, to make detailed measurements of the analyzing power of ^{208}Pb foils at 14 MeV [14,15]. Their measurements were the first to convincingly show the reduction in analyzing power from the nuclear size effect, in agreement with the calculations of Unginčius *et al.* [16]. These measurements are consistent, within their approximately 3% statistical uncertainty, with the dependence of the analyzing power on target thickness arising entirely from double scattering in the target foil, with no net polarization dependence in the second scattering. These double-scattering events must belong to one of two categories, viz., (1) a first scattering very close to 90° followed by a second scattering making the remainder of the total large scattering angle or (2) a first relatively large-angle scattering followed by a second relatively small-angle scattering completing the net large scattering angle (or vice versa). The very thin target foils, and the strong dependence of the differential cross section on angle, effectively restrict events from other than these two classes from significant contributions at few-MeV energies. Only events from category 2 above have useful analyzing power.

Detection of Mott-scattered electrons at a few MeV for precision electron transverse polarization measurement is not experimentally simple, as a quick examination of the relevant cross sections and analyzing powers reveals. Scattering foils with high atomic number, Z, must be used to provide a large spin-orbit effect. The analyzing power is greatest at large scattering angles, while the cross section drops dramatically at larger scattering angles—facts which become ever more pronounced with increasing electron energy. As a result, for every large-angle scattering event providing useful polarization information, a much larger number of electrons scattered at smaller angles are also generated. If one detects only electrons independent of their origin, it is essentially impossible to assure that a detected electron originated from a single or double large-angle scattering in the target foil, as opposed to a scattering in the target foil followed by scattering from the apparatus walls, etc. Since each scattering is primarily elastic or quasielastic, the scattered electron energy is not a very useful discriminant, compared with the percent level energy resolution of commercial scintillating materials often employed for detection of MeV energy electrons (see Sec. VII). Thus MeV energy Mott scattering asymmetry measurements generally include an uncertain and potentially significant contamination from the detection of electrons which did not arise from a single or double elastic scattering in the target foil, and which have a very different scattering asymmetry.

With the high average current available from contemporary polarized electron sources, precision experimental study of Mott polarimetry at accelerator energies in the MeV range becomes practical. Beams from these accelerators have rf time structure, offering the prospect of time-of-flight (TOF) discrimination against electrons that do not originate from the primary scattering foil. The rf time structure and high average beam current make continuous precision monitoring of the beam current and position on the target foil possible. Optical transition radiation (OTR) provides a visible signal with a nonsaturating intensity directly proportional to the local current density incident on the scattering foil, and can be measured continuously for each polarization state during a polarization measurement. Finally, the scattering foils may be considerably thicker than those used at lower energies without introducing overwhelming plural-scattering problems.

Along with these experimental advantages, calculation of the Sherman function with good precision at MeV energies is also practical. This calculation, and a discussion of the many small effects that must be considered, are thoroughly discussed in Sec. III [17,18]. Screening effects are very small at few-MeV energies, while the energy is still low enough that nuclear size effects are also quite small [16,19]. Each of these effects can be calculated with ample precision at the beam energies in question, and contribute very little to the uncertainty in the calculated Sherman function. Exchange scattering is no greater than ≈0.1%, and inelastic scattering in the target foil makes a negligible contribution. The two leading-order radiative corrections, vacuum polarization and self-energy, each of order $\alpha(\alpha Z)$, increase with both Z and energy and are difficult to calculate. They are, however, believed to be of comparable magnitude and opposite sign, as discussed later, leading to some cancellation. The vacuum polarization contribution can be calculated in a reasonable approximation, and is ≈0.4% at our 5-MeV beam energy [17,18]. The total radiative corrections give the largest contribution to the theoretical uncertainty in the Sherman function in the few-MeV energy range, and are estimated to be no greater than ≈0.5%. By measuring the Mott asymmetry from foils of several different atomic numbers and at several different energies it may be practical to place meaningful bounds on this theoretical uncertainty.

These favorable experimental and theoretical considerations led us to develop a Mott polarimeter capable of high statistical precision measurements, which was optimized for a 5-MeV electron beam, the nominal value at the Continuous Electron Beam Accelerator Facility (CEBAF) injector. The 5-MeV polarimeter we describe here has been in use for over 20 years, and has proven to be a readily available, easily used, and reliable monitor of beam polarization in the low-energy region of the injector. For beam energies now reaching 11 GeV, the beam polarization is not measurably degraded during multiple acceleration passes through the full CEBAF accelerator, and remains entirely in the horizontal plane in both the polarized injector and the experimental halls, despite the intervening vertical bends to separate and recombine the beams from different passes through the linear accelerators [20]. Thus the polarization measured in the low-energy region of the injector is directly relevant to the polarization measured at the final energy in the experimental halls over the full energy range of the present accelerator.

Since our original development of this polarimeter, significant improvements to the shielding, detectors, electronics, time-of-flight system, and beam dump have been made, resulting in the current version of the polarimeter presented below. A very early result reported asymmetry measurements from foils of three different *Z*s (29, 47, and 79) in reasonable agreement with expectations, as well as OTR measurements showing that the beam profile was independent of the beam polarization to a high degree [21]. Detailed measurements of a beam with constant polarization at three different beam energies (2.75, 5.0, and 8.2 MeV) made with the original polarimeter with the addition of time-of-flight background rejection have been presented, along with fits to the asymmetry versus target foil thickness at each energy using a semiempirical model based on Wegener's study of the double-scattering problem [22,23]. The entire three-energy data set was fit very well with this model, as shown in Fig. 1, and is consistent with the polarization at all three beam energies being the same within about 0.3%. It is worth noting that foil thicknesses spanning a factor of 100, from 0.05 to 5 μm, were used in these measurements. Using an unpolarized beam, it was determined that the instrumental asymmetry of the polarimeter was $(4 \pm 6) \times 10^{-4}$. Finally, it should be noted that no radiative corrections were included in the computation of the Sherman function at these three energies. Given the dependence of the leading-order radiative corrections on energy, this result provides strong circumstantial support that the net effect of these corrections largely cancels, as theoretically anticipated.

One other polarimeter operating in the MeV range at an accelerator has been reported [24]. This device was operated between 1 and 3.5 MeV at the MAMI microtron accelerator at Mainz. It employed two double-focusing spectrometer magnets followed by scintillation detectors, with a fixed scattering angle of 164°, corresponding to the maximum analyzing power at 2 MeV. They reported a reproducibility better than 1% in their asymmetry measurements, and they believe they reach an absolute accuracy for the measured polarization of about 1%.

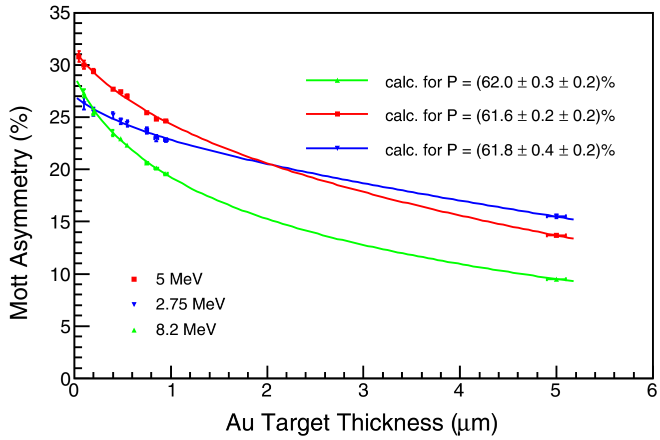

FIG. 1. Asymmetry vs foil thickness measured at three different energies with the original version of the polarimeter. The fits to the three data sets (measured scattering asymmetry vs target foil thickness) are based on the semiempirical model developed by Steigerwald [22]. The fit intercept at zero foil thickness, along with the theoretically calculated Sherman function, then determines the beam polarization.

II. MOTIVATION AND METHODS

The motivation for our MeV Mott polarimetry studies has been to reduce the uncertainty in the measured polarization of longitudinally polarized electron beams used for parity-violation studies at CEBAF. This is because uncertainty in the beam polarization is the dominant uncertainty in the measured parity-violating asymmetry in the scattering of longitudinally polarized electrons from nuclear or electron targets. The high-precision Mott polarimeter described here not only provides an independent measurement of the beam polarization from the injector, but is a very useful instrument to normalize the polarization measured by various polarimeters in the experimental halls [25]. A meaningful reduction in the uncertainty of the electron-beam polarization will directly impact the physics interpretation of high-energy parity-violation measurements.

In this paper we have employed methods to test and improve both the accuracy and precision of the measured beam polarization. The accuracy was improved by performing theoretical calculations of the Sherman function, applying statistical analyses to the analyzing power dependence on polarimeter target thickness, and developing GEANT4 simulations to model and validate the analyses. The precision of the polarimeter was investigated by detailed examination of the dependence of the measured physics asymmetry on the detector signals that are recorded to isolate the polarization dependent Mott elastic signal, as well as a number of potentially important systematic effects.

For a given beam polarization the measured experimental asymmetry is proportional to the analyzing power of the polarimeter. Theoretically, the analyzing power of Mott scattering from a single atom is known as the Sherman function. Experimentally, in a real target foil, an electron may scatter from more than a single atom, leading to a lower analyzing power known as the effective Sherman function. The usual way to determine the effective Sherman function for a particular foil thickness and unknown polarimeter is to measure the asymmetry for several foil thicknesses and extrapolate to the zero-thickness single-atom value. The extrapolated asymmetry in conjunction with the theoretical Sherman function is then used to determine the beam polarization and also calibrate the effective Sherman function of each target foil tested.

Data obtained over two run periods (referred to as runs 1 and 2) were used for this paper. The two runs were performed six months apart, each run employing a similar but physically different photocathode to produce the polarized beams. Systematic studies of possible sensitivities of the results on various beam parameters were performed during both run periods. In the sections that follow, the purpose and methods are discussed for each significant aspect of the measurements, and the corresponding systematic and statistical uncertainties associated with each are analyzed.

III. CALCULATION OF THE THEORETICAL SHERMAN FUNCTION

For electron scattering at few-MeV energies, the scattering potential is modified from the Coulomb field of a point nucleus by four effects. In order of importance for our case, these are (i) the finite size of the nucleus, (ii) screening of the nuclear Coulomb field by the atomic electrons (essentially only those in the K shell), (iii) the exchange interaction between the incident electron and the atomic electrons, and (iv) inelastic scattering of the incident electron on the atomic electrons. Each of these effects reduces the Sherman function below that calculated for a point nucleus. These four effects were calculated with the code ELSEPA [26,27], which does relativistic partial-wave calculations of the differential cross section and spin-polarization functions with state-of-the-art potentials. In addition to these effects, bremsstrahlung and QED radiative corrections must also be considered. We discuss the impact of each of these effects below. Considerable detail on the calculation of the Sherman function for our experiment is given in a recent paper by Roca-Maza [18].

For calculations of the effect of nuclear size on the polarization functions and differential cross section, the nuclear charge density was modeled by a two parameter Fermi function. As the de Broglie wavelength of a 5-MeV electron (226 fm) is very large compared to the rms charge radius of ^{197}Au (5.437 fm in the two parameter Fermi function model), greater detail for the nuclear charge distribution is safely neglected (cf. Figs. 1 and 7 in Ref. [18]). Indeed, the Sherman function calculated with the two parameter Fermi function agrees with that calculated using a multiparameter self-consistent mean-field model of the nuclear charge distribution to within 0.1% in the region of interest. For 5-MeV electrons on ^{197}Au, the nuclear size effect reduces the Sherman function of a point nucleus by 1.4%, with an uncertainty less than 0.1%.

To calculate the effects associated with atomic electrons, the most accurate electron densities obtained from self-consistent relativistic Dirac-Fock calculations have been used [28]. For the calculation of exchange scattering, the Furness-McCarthy exchange potential was used [29]. Inelastic scattering was calculated using a potential proposed by Salvat [30]. The effects of screening, exchange, and inelastic scattering on the Sherman function in our kinematic region are all very small. Specifically, for 5-MeV electrons on ^{197}Au at 172.6°, screening is about 0.02%, and exchange is about 0.01%. Inelastic scattering is 0.03% for 1-MeV electrons, and is expected to be smaller at higher energies. The uncertainties in each of these corrections are no greater than 10% of the corrections. The details are covered in Ref. [18].

We are unaware of any complete calculation of the two lowest-order radiative corrections to Mott scattering, vacuum polarization, and self-energy, each of order $\alpha(\alpha Z)$. The vacuum polarization correction can be calculated with the aid of the Uehling potential, as has been done recently by Jakubassa-Amundsen [31]. As the Uehling potential has the same sign as the Coulomb potential, the vacuum polarization effect increases the analyzing power. At our 5-MeV energy, the calculated effect is +0.39%. The size of this correction increases with energy.

While the lowest-order self-energy terms have not been calculated for Mott scattering, a subset of these terms has been calculated for the related process of radiative electron capture by a bare heavy nucleus, which is the time-reversed analog of the photoelectric effect [32]. As with the Mott calculation, the vacuum polarization terms were evaluated with the aid of the Uehling potential. The self-energy correction was calculated only for the part involving the bound-state electron wave function, omitting the part involving the continuum-state wave function. The calculations were done for three incident heavy-ion (U^{92+}) energies. In all cases, the magnitude of the corrections increased with energy, the vacuum polarization terms were positive, and the self-energy terms calculated were negative and about a factor of 3 larger than the calculated vacuum polarization terms. This gives some cancellation between the vacuum polarization and self-energy terms for the total first-order radiative corrections. Given the similarity of the vacuum polarization and self-energy effects in both radiative electron capture and Mott scattering, it is widely believed that these two terms will be of opposite sign and similar magnitude in Mott scattering.

There is also a correction due to bremsstrahlung. One calculation of this correction at several energies between 128 and 661 keV, and at five angles in 30° steps to 150°, has been reported [33]. The calculated correction increased the measured polarization at all points. The correction decreased with energy for the central angles and increased with energy at both forward and backward angles. The increase was more pronounced at forward angles than backward angles. The correction calculated at 661 keV and 150° was +1.18%. These calculations are not useful for making any projection about the

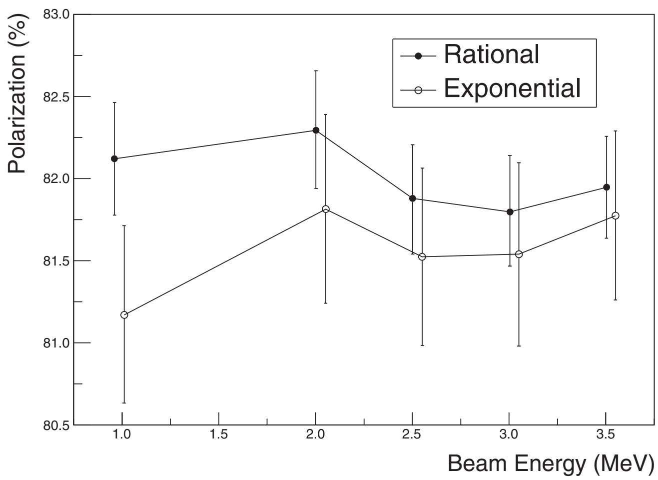

FIG. 2. Polarization determination for several energies using two different fit functions (excerpted from Ref. [24]). Uncertainties ($\pm 2\sigma$) are from the fit only.

bremsstrahlung corrections at our beam energy and scattering angle, but it appears possible to calculate this correction for our conditions, using the complex expressions presented in the paper. If this correction remains positive with our kinematics, this will counter the anticipated net negative effect of the first-order radiative corrections.

The ^{197}Au nucleus has a spin of 3/2 and a relatively small magnetic moment of $\approx$0.147 nm. Jakubassa-Amundsen [31] has calculated the effect of magnetic scattering in the case of Pb^{207}, with its much larger magnetic moment of 0.593 nm, and has shown that it is completely negligible below energies of $\approx$100 MeV and angles less than $\approx 178^\circ$ [31]. We therefore believe that magnetic scattering is negligible for Au^{197} with our kinematics and make no correction for the effect. Finally, we have made no correction for recoil effects, which we believe to be small. The β of the recoiling gold nucleus is $\approx 0.5 \times 10^{-5}$ for 5-MeV incident electrons.

Two experiments have previously reported Mott scattering polarization measurements over a range of energies between 1.0 and 8.2 MeV. The first of these reported measurements at three energies between 2.75 and 8.2 MeV, with a range of foil thicknesses spanning a factor of 100, from 50 nm to 5 μm [22]. These data were fit with a single semiempirical function based on Wegener's study of double scattering [23]. The results, shown in Fig. 1, show the same polarization at all three energies within about 0.3%. These results included no corrections for QED radiative effects or bremsstrahlung. The second measurement covered the energy range between 1.0 and 3.5 MeV and showed a polarization consistent with a constant value to within about 0.5%, as shown in Fig. 2 [24]. Again, no corrections for QED radiative effects or bremsstrahlung were made.

These two experiments, using different polarimeters and conducted by different groups at different laboratories, present strong circumstantial evidence that the total effect of QED radiative corrections, bremsstrahlung, and recoil is no larger than about 0.4% over the full energy range measured. There is good reason to believe that the vacuum polarization correction, known to be positive, is a fraction of the self-energy correction, and there is some evidence that the bremsstrahlung correction may have the same sign as the vacuum polarization term over this kinematic range. The vacuum polarization correction calculated with the aid of the Uehling potential is known to increase significantly with energy over the range in question, and the self-energy terms calculated for radiative recombination also increase with energy. It therefore appears that the net effect of these corrections nearly cancels over the full energy range measured. The QED corrections are proportional to Z, and it has been demonstrated practical to measure Mott scattering with different Z foils with our polarimeter. In the future, such measurements may lead to improved limits on the total magnitude of these corrections.

Our estimate is that the net effect of the QED corrections, bremsstrahlung, and recoil is negligible, with an uncertainty of about 0.4%. For a nominal electron-beam kinetic energy of 5.0 MeV and a scattering angle of 172.6°, the theoretically calculated Sherman function is 0.5140 ± 0.0026, having increased the total uncertainty to 0.5%.

IV. POLARIZED ELECTRON INJECTOR

The CEBAF polarized electron injector comprises several subsystems, including a dc high voltage electron gun with a photoemission cathode, a laser system for illumination of the photocathode, a group of electromagnetic elements to orient the spin of the electron beam, several rf cavities to temporally shape the individual electron bunches and accelerate them to several MeV, a number of conventional steering and focusing magnets, and beam diagnostic elements which allow us to establish and maintain the desired beam conditions. A plan view of the injector, from the electron gun to downstream of the Wien filter spin orientation section, is shown in Fig. 3.

The inverted-insulator dc high voltage electron gun has a load lock to allow exchange of photocathodes without breaking the ultrahigh vacuum in the gun [34]. The photocathode is a strained multilayer $\mathrm{GaAs} - \mathrm{GaAs}_{1-x}\mathrm{P}_x$ structure which delivers $\approx$86% longitudinally polarized electrons when illuminated at normal incidence by 100% circularly polarized light of near-band-gap photon energy [35]. Any small residual linear polarization of the optical beam does not result in any polarization of the electron beam. Under normal CEBAF operating conditions, the photocathode is illuminated with laser light from three rf gain-switched diode lasers, each delivering a pulse train at 499 MHz, which is one-third of the 1497-MHz fundamental rf frequency of the CEBAF accelerator [36]. For the work reported here, only a single laser was used. This laser was operated on the 16th subharmonic of 499 MHz, producing a train of electron bunches at a 31.1875 MHz, and thus providing a separation of 32.0641 ns between bunches. Producing an optical pulse train at this low frequency was accomplished by a digital laser gain-switching technique, which produced optical pulses largely free of secondary pulses [37]. The fundamental laser wavelength is 1560 nm, which was frequency doubled to 780 nm, providing maximum electron polarization from the photocathode. The linear polarization of the doubled laser beam was converted to circular polarization with a Pockels cell which rapidly reverses the beam helicity.

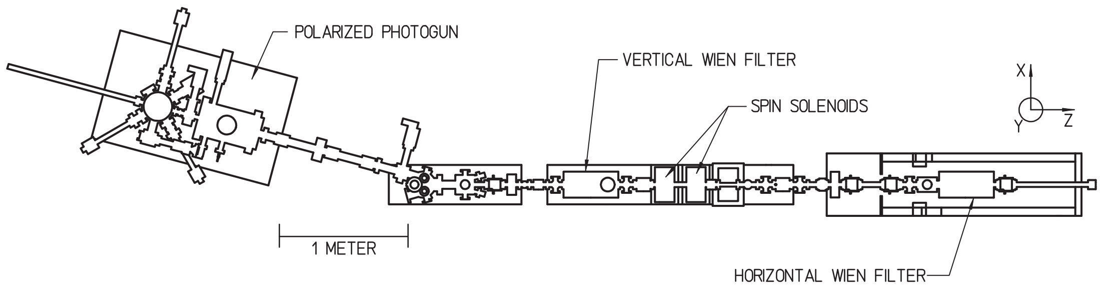

FIG. 3. This plan view of the first part of the CEBAF injector highlights the polarized photogun followed by the electromagnetic elements that determine the spin direction of the beam. The orientation of the electron polarization is longitudinal as the beam exits the photogun.

A high-quality zeroth-order mica half-wave plate before the Pockels cell allows the sense of the circular polarization, and hence the electron-beam polarization, to be reversed while leaving the Pockels cell voltages unchanged.

Jefferson Lab polarized electron experiments generally require longitudinally polarized electrons. There is a very large polarization precession in the horizontal plane of the CEBAF accelerator between the polarized electron source and the experimental targets, requiring the polarization of the beam exiting the electron injector to be properly oriented to give maximum longitudinal polarization at the experiment. This orientation is done by two Wien filters and two nominally identical solenoids between them. Small quadrupoles allow correction of the electron-optical astigmatism of the Wien filters. This scheme allows the beam exiting the second Wien filter to have any spin orientation while keeping the beam properly focused. The Wien filters are described in detail in Grames *et al.* [25]. They are capable of providing a 90° spin rotation to a 130-keV electron beam, the current electron gun operating voltage. The two solenoids between the Wien filters allow reversal of the beam polarization without altering the focusing through the injector, which is valuable for understanding polarization associated systematic effects, particularly in experiments such as parity-violation studies, which must measure very small asymmetries. The complete polarization orientation system, including the details of its electron optics, is described in Grames *et al.* [38].

Magnetic solenoids with their magnetic-field axis colinear with the beam axis both rotate any transverse component of electron spin passing through them about the beam axis (leaving any longitudinal component undisturbed) and focus the beam. The spin rotation is proportional to the magnetic-field integral of the solenoid, while the focusing is proportional to the integral of the square of the field through the solenoid. A compound solenoid with a pair of magnetically separated equal and opposite excitation coils (a so-called counterwound or Stabenow configuration) produces a net beam focusing from the net square of the field integral, but no net spin rotation from the net zero-field integral. All solenoids in the CEBAF injector following the Wien filter section are of this type. This assures that the spin orientation established in the Wien filter section is maintained through the injector.

The two Wien filters and the associated solenoids orient the electron spin for all CEBAF experiments, as well as providing spin orientation reversals for systematic error cancellations. We conducted two independent series of Mott polarization measurements from two different photocathode sources (runs 1 and 2). In the run 1 measurements, the vertical Wien filter oriented the electron spin vertical, and the two solenoids rotated the spin to the horizontal direction. This provided an electron beam maximally polarized in the horizontal plane at the Mott polarimeter, and thus nominally gave a maximum "up-down" asymmetry and a zero "left-right" asymmetry in the polarimeter detectors. In run 2, the vertical Wien filter again oriented the electron spin vertical, but the two solenoids were set to only focus the beam, without polarization rotation, and thus gave a maximum left-right asymmetry with a zero up-down asymmetry. In both runs the second horizontal Wien filter remained unpowered.

The electrons for the Mott experiment are accelerated first to 500 keV by a normal conducting accelerating cavity and then by two five-cell superconducting (SRF) accelerating cavities designed to maximally accelerate electrons moving at the velocity of light. For the Mott measurements, these cavities produced a beam of 5-MeV nominal energy, accelerating electrons from $\beta = v/c$ of 0.86 to $\beta = 0.996$. Since $\beta < 1$, care must be taken to assure that the phase of the rf power to the SRF cavities, which are designed for accelerating $\beta = 1$ beams, produces both a high-energy gain and a minimal energy spread.

The beamline between the SRF cavities and the Mott polarimeter is shown in Fig. 4. The magnets through this section are conventional quadrupoles, air core steering correctors, and a dipole. These magnets do not have any significant effect on the polarization orientation. The dipole is used to deflect the beam to a spectrometer at $-30°$, to the Mott polarimeter at $-12.5°$, or to a well-instrumented beamline leading to various other injector energy experiments at 25°. Following the two experimental runs, the vertical bending component of the magnetic field through this region, typically $\approx$0.5 G, was measured. This information, coupled with details of the corrector fields, quadrupole strengths, and the centering of the beam as it passed through the quadrupoles and the position monitors, led to a detailed calculation of the beam kinetic energy entering the Mott polarimeter. The resulting beam energies and uncertainties for the two runs are described in detail in a Jefferson Lab technical note [39]. The beam kinetic energies were 4.806 ± 0.097 MeV for run 1, and 4.917 ± 0.013 MeV for run 2.

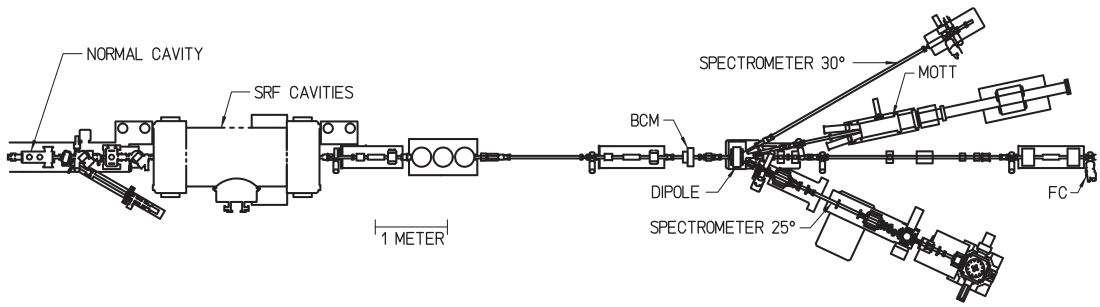

FIG. 4. Plan view of the injector illustrating the rf accelerating cavities, the 12.5° beam line through the Mott polarimeter, the spectrometer beam lines at −30° and 25°, and the straight beam line leading to the rest of the CEBAF injector including an rf cavity beam current monitor (BCM) and a Faraday cup (FC).

The beam emittance was measured following run 1 by the quadrupole scan method using the first quadrupole in the beam line and a downstream wire scanner. The horizontal normalized rms emittance was about 0.56 μm, and the vertical normalized rms emittance was about 0.4 μm. These emittances, though small, reflect the relatively large illuminated area of the photocathode as used in a recent parity-violation study [40]. Given these small emittances, they were not remeasured in run 2. These emittances resulted in beam sizes of typically ≈0.5-mm rms at the Mott scattering foil, and similarly small diameters throughout the entire beam line.

V. DESIGN OF THE POLARIMETER

The polarimeter vacuum chamber, shown in Fig. 5, is composed of three segments—a scattering chamber containing the target foils, apertures, and detector ports; an extension section providing a vacuum pump port; and a long drift chamber ending in a beryllium and copper beam dump structure. The polarimeter is connected directly to a beam port 12.5° off the main accelerator beam line, with no intervening vacuum windows. The beam is steered to the polarimeter by a dipole magnet. When not in use, the polarimeter is isolated with a

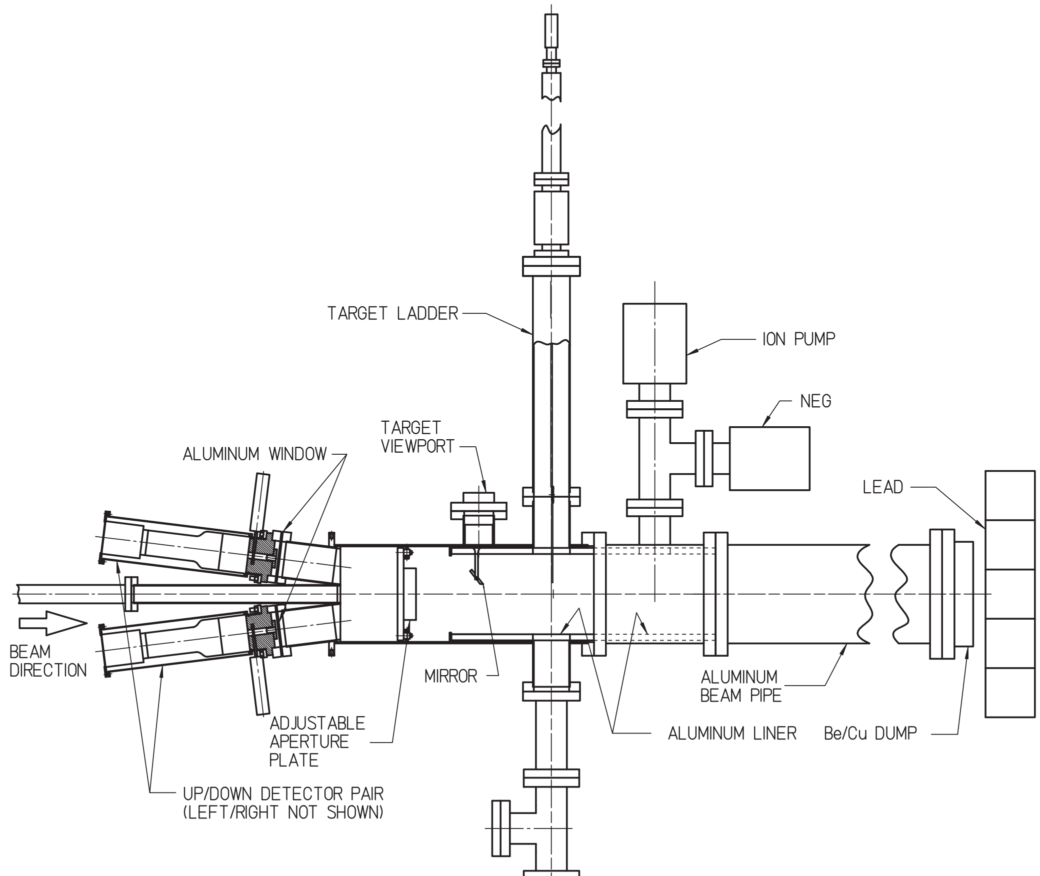

FIG. 5. Elevation view of the Mott polarimeter, including the beam line from the dipole magnet which steers the beam into the polarimeter.

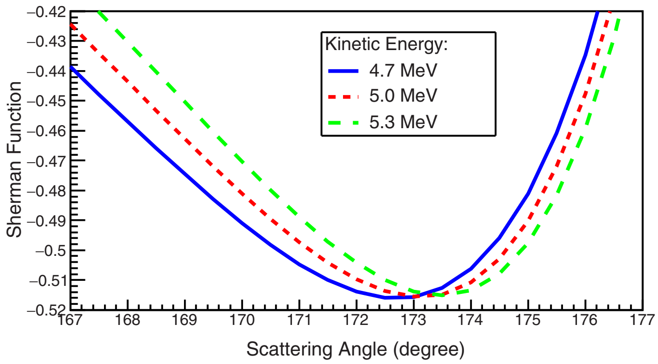

FIG. 6. Sherman function for three electron-beam kinetic energies.

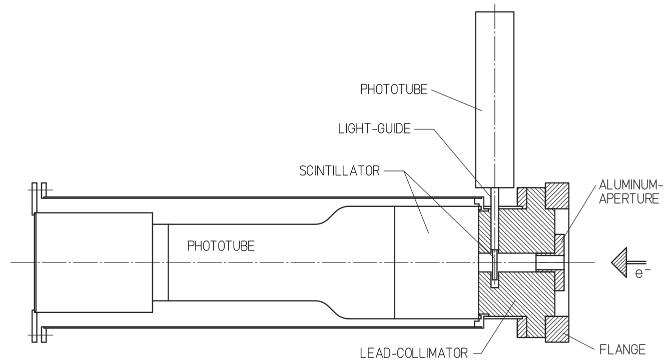

FIG. 7. Mott detector assembly illustrating each of the collimators, scintillators, and phototubes which comprise the coincident detection of a scattered electron.

beam line vacuum valve. Vacuum in the chamber is maintained below a nominal pressure of $\approx 10^{-7}$ Pa by several deionized ion pumps and a non-evaporable getter (NEG) pump. The internal surfaces of the chambers have a 12.7-mm-thick aluminum liner downstream of the target foils to reduce both backscattered electrons and the photon background in the detectors.

The scattering chamber has four detector ports, each centered on a scattering angle of 172.6° and separated by 90° in azimuth, with two in the horizontal plane and two in the vertical plane, allowing simultaneous measurement of both transverse components of the beam polarization. Four internal knife-edge apertures of 4.87-mm diameter are precisely machined in a 25.4-mm-thick aluminum plate, centered on a 25.4-mm-diameter aperture to pass the incident beam. This plate is mounted in turn on a 12.7-mm-thick aluminum plate which covers very nearly the entire cross section of the scattering chamber. The solid angle subtended by each aperture is 0.23 ms. Using precision survey techniques, the 25.4-mm-thick plate was positioned so the four apertures were centered on the 172.6° scattering angle lines between the center of the scattering foil and the detector packages. The 5.0-MeV Sherman function for a point nucleus was originally calculated to be maximum at the 172.6° angle. This angle is somewhat greater when the nuclear size effect is included. Recent calculations place the Sherman function maximum, corrected for the nuclear size, at about 173.0°. It is worth noting that the Sherman function is within 0.995 of its maximum value in this case over about 1.8°. The individual apertures noted below, in each channel, span about 0.9°. Scattered electrons that pass through an aperture enter a detector package through a 50-μm aluminum window, immediately followed by 9.7-mm-diameter aperture in a 12.7-mm-thick aluminum plate centered on the 172.6° scattering angle. Figure 6 shows the Sherman function for three electron-beam kinetic energies [18].

The target ladder is mounted on a bellows sealed translation mechanism with 600 mm of travel, which is driven by a stepper motor. It has 16 target foil mounting positions, each with a 25.4-mm-diameter clear aperture. One of these is left open intentionally, and a second contains a chromox beam viewscreen, leaving 14 positions available for scattering foils. Fourteen gold foils were installed, although four of these foils had nonstandard mountings and were not used for the measurements reported here. The target ladder assembly is thoroughly described in a JLAB technical note [41]. Details of the target foils are discussed in the Appendix. Finally, a port with an optical window is located on the side of the chamber behind the target foil plane, allowing the target foil to be viewed by a polished stainless-steel mirror. OTR propagating backward at about 167° provides a visible image, viewed by a CCD camera, of the beam incident on the scattering foil. This provides an accurate, nonsaturated real-time image of the beam profile at the target foil.

A 2.5-m section of a 20-cm-diameter aluminum vacuum tube terminating in a beam dump follows the vacuum extension section. The dump is an 18.4-cm-diameter, 6.35-mm-thick disc of Be metal, affixed to a water-cooled reentrant copper flange structure by screws. Beryllium offers excellent thermal conductivity, and a low ratio of radiative to collisional electron energy loss. The use of Be offers high beam power handling capability, and minimizes both electron backscattering and photon production. Operation with 75-μA beam current (375-W beam power) has been conducted with this dump, which is designed to operate with a 1-kW beam power limit.

Figure 7 shows one of the four identical detector packages. Each package contains two plastic scintillation detectors behind a lead and an aluminum collimator. The first "ΔE" detector is a 1.0-mm-thick, 25.4-mm square plastic scintillator, while the second "E" detector is a 76.2-mm-diameter by 62.6-mm-long plastic scintillator. The ΔE scintillator is optically connected to a 25.4-mm-diameter phototube (Hamamatsu R6427) by an acrylic lightguide glued to both the scintillator and the phototube, while the E scintillator is directly glued to the face of a 76.2-mm phototube (Hamamatsu R6091). The surfaces of the E scintillator were painted with a diffuse reflector to improve the optical photon transport to the photomultiplier cathode. The entire four detector package was enclosed in at least 10-cm-thick lead shielding constructed from standard 51 × 102 × 203-mm lead blocks.

VI. DATA ACQUISITION SYSTEM

The electronic signal processing circuitry for the ΔE and E signals of one of the four arms of the data acquisition

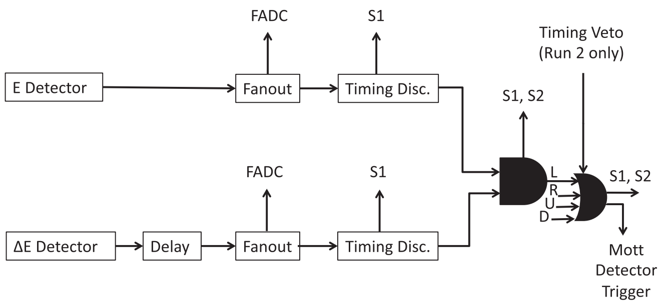

FIG. 8. Electronic signal processing of the ΔE and E signals (the "left" of four detector arms).

system (DAQ) is shown in Fig. 8. The photomultiplier high voltages for each of the four ΔE and E detectors were set to produce nominal -200-mV signal pulses. A Mott scattered electron deposits about 10 keV in the ΔE scintillator, and the remainder of the energy in the E scintillator. The ΔE and E signals are sent to linear fanouts. Copies of each signal are sent to a multichannel flash analog to digital converter (FADC) and to constant fraction timing discriminators. The discriminator outputs are sent to both a scalar (S1) and an AND logic module to generate a ΔE-E coincidence for that detector arm. The ΔE detector signal has a faster rise time than the E detector signal, so a delay was added to the ΔE signal line to improve the timing jitter of the coincidence signal. The ΔE-E coincidences for each of the four arms (L, R, U, and D) are sent to two scalers, S1 and S2. The S1 scaler counts only when the beam polarization is stable between helicity reversals and is tagged by the sign of the polarization. The S2 scaler is free running and counts whenever the DAQ is running.

The four ΔE-E coincidence signals are combined in an OR logic module. Two outputs from this module are read out by scalers S1 and S2 to count the total number of events in the four detector arms. Another output triggers the DAQ event read out.

During run 1, we began with a conservative low discriminator threshold (-25 mV) for the E detectors. Detailed studies showed that we could raise these discriminator thresholds considerably, thus reducing the counting rate and dead time meaningfully, without impacting the results. This higher threshold (-100 mV) was used for the second half of run 1 and throughout run 2.

During run 2, a hardware time-of-flight veto was added (see Fig. 8) to reduce the background events associated with the beam dump. The timing veto signal with a width of 12 ns, synchronized to the 31-MHz laser-rf signal, was adequate to eliminate electrons backscattered from the dump from reaching the scattering foil and subsequently scattering into a detector arm. In this way, we eliminated this contribution to the DAQ dead time and were thus able to increase the effective event rate from the scattering foil.

We used a virtual machine environment (VME)-based data acquisition system. The VME crate contained the S1 and S2 scalars, the FADC and time to digital converter (TDC) modules, and a system trigger interface and distribution module. The helicity control board is located in

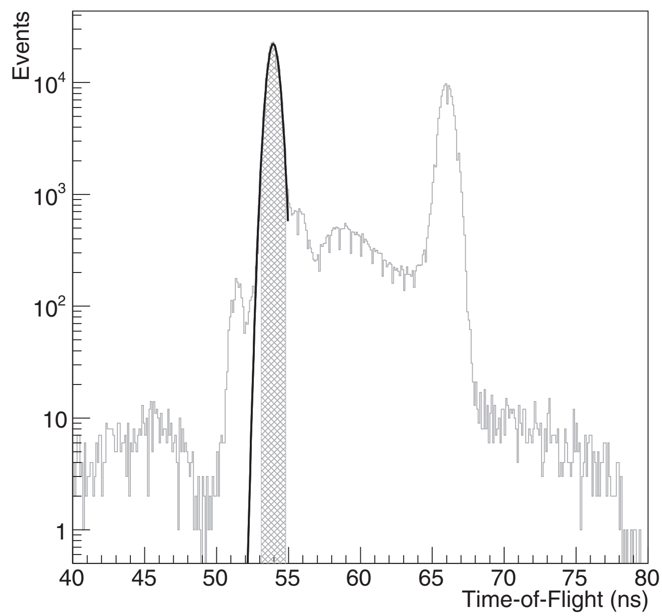

FIG. 9. A typical time-of-flight distribution of Mott coincidence triggers. Mott events from the scattering foil appear at ≈54 ns, while electrons backscattered from the beam dump are detected at ≈66 ns. Data from run 1 with the 355-nm foil.

a separate electrically isolated VME crate distant from the detector electronics and DAQ. A thorough description of the scintillation detectors, detector electronics, DAQ, and helicity control system is given in a JLAB technical note [42].

Measurement of the TOF distribution of coincidence events was done using two channels of the TDC. The TDC common start signal is generated by a Mott detector trigger. One stop signal is generated by a suitably delayed Mott detector trigger, and the other stop signal is from the 31-MHz laser-rf signal which defines the beam pulse. The difference between these two TDC channels generates the TOF distribution unaffected by any jitter in the generation of the TDC common start signal. The TDC has a full scale of 134 ns, and a resolution of 34 ps/channel. A typical TOF distribution is shown in Fig. 9.

The standard deviation of the TOF distribution around the elastic peak is 0.73 ns. The time for a speed of light particle to move from the scattering foil to the dump is 6 ns, and thus a dump peak is detected 12 ns after the elastic peak. When applied, the timing veto removes events between 62 and 74 ns, which includes events associated with the beam dump. The remaining events that occur in the TOF distribution arise from electrons scattering from vacuum chamber surfaces which reach the detectors out of time with the desired Mott events.

The FADC is a 12-bit analog-to-digital converter (ADC) that samples at 250 MHz. Eight FADC input channels with a -500-mV full range are used for the ΔE and E photomultiplier signals. For every Mott scattering event, 50 samples from each of the eight FADC channels, equally spaced in time, are read out. The first ten samples in the E signal occuring before the Mott event arrives are used to calculate an average

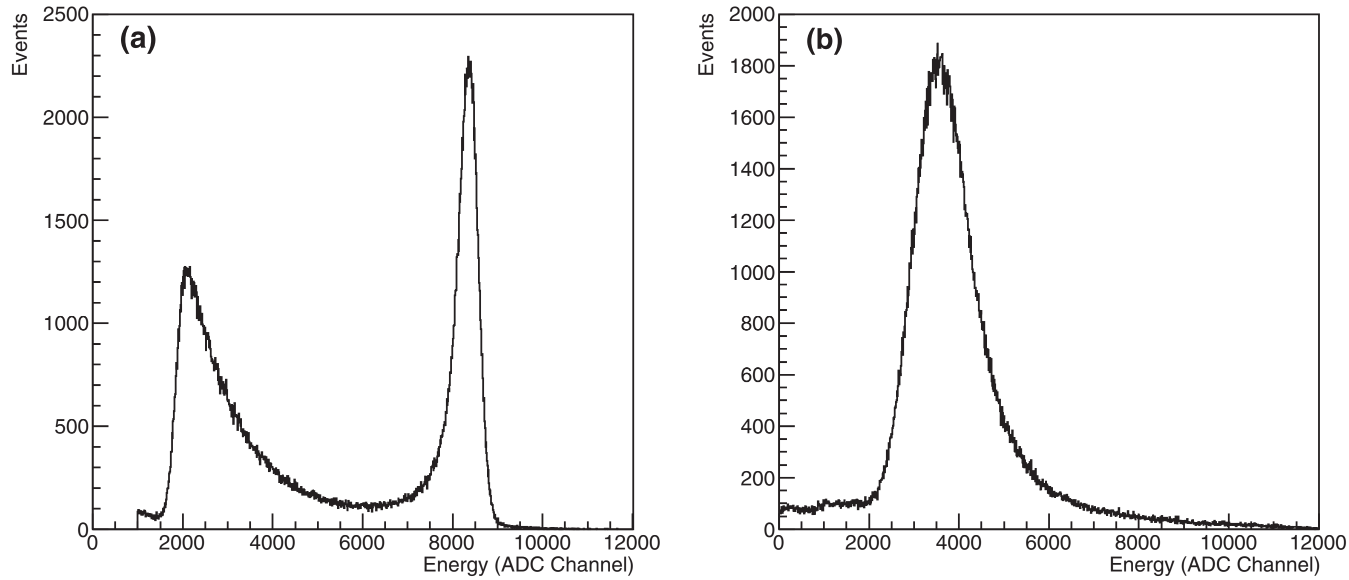

FIG. 10. Typical histograms of the (a) E and (b) ΔE detectors. The E threshold was set to -25 mV for these data and no timing cut was applied. Data from run 1 with the 355-nm foil.

pedestal of the FADC. A value proportional to the total energy deposited in the E detector is then calculated by summing the pedestal subtracted signal over the remaining 40 ADC samples. Examples of representative histograms are shown in Fig. 10. TOF histograms for each detector are also generated as in Fig. 9.

VII. DATA REDUCTION

For each individual Mott measurement the DAQ generates a raw data file, which is decoded into a ROOT tree [43]. The Mott analysis code consists of three loops which are executed sequentially. In the first loop, the time-of-flight and energy spectra are fit in order to isolate elastic events from the target foil. In the second loop, these events are sorted by their beam helicity to compute the experimental asymmetries and determine helicity averaged rates. In the third loop, scaler data are used to determine the integrated beam current charge asymmetry and DAQ dead time.

A. Loop 1: Identifying Mott scattered coincidence events

The elastic peak of each detector's TOF spectrum is fit with a Gaussian using the default ROOT TH1 class χ^2 least-squares fitting routine that uses MINUIT and the MIGRAD minimizer. The fit is restricted to the 49- to 55-ns range, shown as the solid curve in Fig. 9. Note that in this figure the TOF veto has not been applied, so events originating from the beam dump are also present, centered at approximately 66 ns. From this fit, the time window for Mott scattering events from the target foil is taken to be -2σ to $+2\sigma$ of the mean Gaussian fit, shown as the hatched area in Fig. 9.

The four E detector spectra, after applying the TOF cut, were then normalized to place the Mott peak of each detector in a standard channel—in our case channel 8000. This was done by linearly shrinking or expanding the raw spectra. In all cases this was a very small change, $\approx$4% in the largest case. The results are shown in Fig. 11, showing that the four E detector spectra are quite similar. This normalization allows us to standardize the cuts to the energy spectra.

The four normalized and TOF-cut E detector spectra are then each fit with a Gaussian. The fit is restricted to ± 500 channels about the central peak bin. Again, the default ROOT TH1 fitter is used. A fit to a left detector energy spectrum is shown in Fig. 12. A "good" elastic scattering event has been determined to lie between -0.5σ and $+2\sigma$ as shown as the hatched area in Fig. 12.

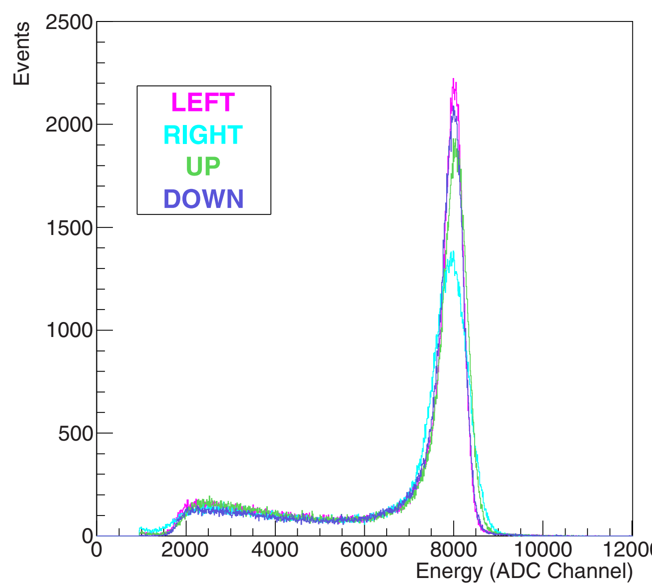

FIG. 11. The superimposed normalized energy spectra of the four E detectors, after the timing cut was applied. Data from run 2 with the 355-nm foil.

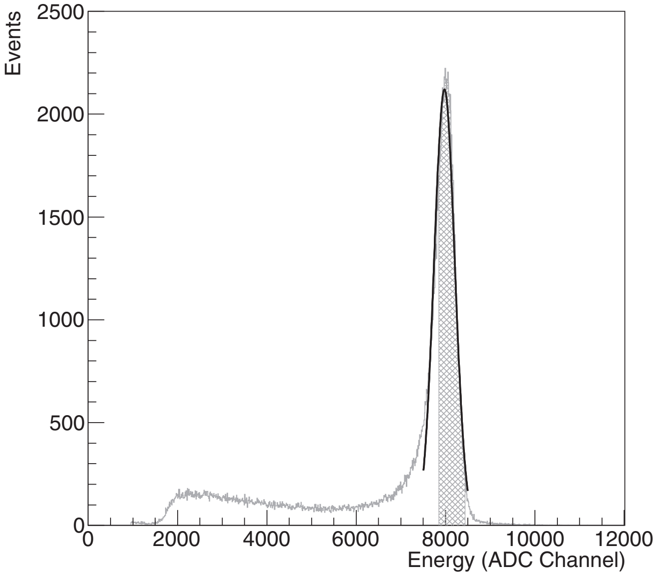

FIG. 12. A Gaussian fit (solid line) to an energy spectrum of the E detector used to define the events used to calculate a Mott scattering asymmetry. Data from run 1 with the 355-nm foil.

Figure 13 shows a contour plot of energy versus time of flight for all Mott events from a particular single Mott measurement, with the energy and TOF cuts shown. The choice of both the TOF and energy cuts is explained in detail next.

B. Loop 2: Computing helicity correlated asymmetries

Establishing the beam helicity and transmitting this information to the Pockels cell high-voltage driver and the Mott DAQ is done with the helicity control board. The helicity control board generates a 0.5-ms "T-settle" signal which indicates when the Pockels cell high voltage is changing between states, followed by a 33.33-ms "T-stable" signal indicating that the Pockels cell voltage, and thus the beam helicity, is stable. Mott events are tagged as good when they occur during the T-stable times. Beam helicities are generated in quartet patterns of either $+ - - +$ or $- + + -$, with the quartet pattern selected randomly. Each of the four entries in a quartet pattern is composed of a single 0.5-ms T-settle time and a single 33.33-ms T-stable time.

With final histograms for the E detectors and the TOF spectra, we calculate the helicity correlated experimental asymmetries using the cross-ratio method [44]. The cross-ratio method cancels to all orders the relative variations in detector efficiencies and solid angles of the two detector arms, and any variation in beam current that might exist between the two helicity states. With "L^+" and "R^+" referring to the events within specified TOF and energy cuts in a pair of opposing detectors for positive incident beam polarization (L^+ and R^+), and similarly for negative polarization (L^- and R^-), the cross ratio r is

$$r = (L^+R^-/L^-R^+)^{1/2}$$

and the quantity N is

$$N = (1/L^+ + 1/L^- + 1/R^+ + 1/R^-)^{1/2}.$$

The asymmetry is then given by

$$A = (1 - r)/(1 + r)$$

with a statistical uncertainty

$$dA = rN/(1 + r)^2.$$

We conducted an extensive study of the effect of varying the energy and TOF cuts on the resulting asymmetry value. The asymmetry showed only a very small dependence on

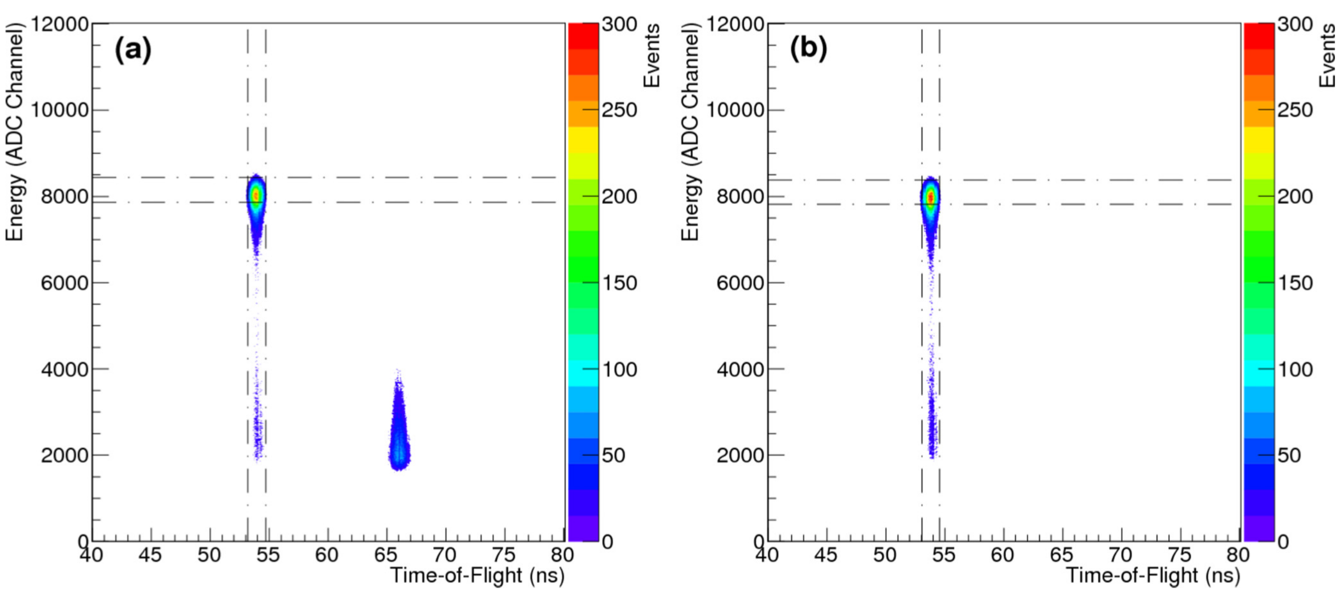

FIG. 13. Energy-time coincidence plots show the distribution of events from a single Mott measurement in (a) run 1 with the 355-nm foil where no hardware TOF veto was applied and (b) run 2 with the 355-nm foil where this hardware veto was applied. In each case the dashed lines indicate the applied TOF and energy cuts that were used to select the events for the calculation of the asymmetry.

the TOF cuts. TOF cuts larger than $\pm 2\sigma$ had essentially no effect on the resulting asymmetry, while $\pm 1\sigma$ gave somewhat smaller asymmetries (though well within $\pm 1\sigma$ of the maximum asymmetry), likely due to the fact that the TOF peak in each detector arm occurred at fractionally different TOF bins due to small cable length differences. With the TOF cut settled at $\pm 2\sigma$, we binned the TOF-cut asymmetries in 0.5σ energy bins between -5σ and $+5\sigma$. The asymmetry within each 0.5σ slice was calculated for the Padé (0,1) and Padé (1,1) functions, described below.

The pulse height spectrum in the E detector spectra (of Fig. 12) is not Gaussian over the full range of the peak. This is primarily because there are mechanisms that generate real or apparent energy loss, but none that generate energy gain. So, for example, imperfect light collection from the scintillator, bremsstrahlung, or Compton scattering leading to undetected photon energy or electron (or positron) escape from the scintillator may all contribute to peak broadening on the low-energy side of the peak. While GEANT4 simulations of the detector package were performed to validate these mechanisms, we have not attempted to precisely model the full energy spectrum for the purpose of defining the analysis. Instead extensive examination of the energy spectra with various functional forms (e.g., Gaussian or Lorentzian) led to the use of energy cuts between -0.5σ and $+2.0\sigma$. We further examined these cuts by systematically shrinking or enlarging them in 10% steps up to 30% and noting the effect these changes had on the uncertainty in the asymmetry. In all cases, at the statistical expense of eliminating events, our choice of cuts led to the smallest uncertainty on the asymmetry, and did not bias the scattering asymmetry. A systematic uncertainty of 0.1% is assigned to the energy cut. Thorough details of the analysis study are described in a JLAB —technical report [45].

The cross-ratio method can also be used to check for any instrumental asymmetries. For example, if r were instead defined as $(\mathrm{L}^+\mathrm{L}^-/\mathrm{R}^-\mathrm{R}^+)^{1/2}$, then the asymmetry calculated would indicate how different the right detector is from the left detector (e.g., detector solid angle, detection efficiency, or discriminator threshold). Alternatively if r were defined as $(\mathrm{L}^+\mathrm{R}^+/\mathrm{L}^-\mathrm{R}^-)^{1/2}$ the calculated asymmetry would indicate a difference in the beam between the two helicity states (e.g. beam current or target thickness variation). The detector and beam instrumental asymmetries for both run 1 and run 2 were less than 1%, affirming the advantageous use of the cross-ratio method to calculate the Mott asymmetries.

C. Loop 3: Computing current dependencies

A fundamental frequency rf cavity (labeled BCM in Fig. 4) was cross calibrated against a precision Faraday cup further down the primary beam line and used to noninvasively monitor the beam current during each scattering asymmetry measurement. The beam generated rf power from the cavity, proportional to the square of the beam current, was processed to provide a voltage signal proportional to the instantaneous beam current. This signal could be cross calibrated against a precision Faraday cup further down the primary beam line. Conversion of this voltage signal to frequency provided a pulse train that was counted to give the integrated beam current over the duration of a single Mott measurement.

As noted earlier, the cross-ratio method of calculating scattering asymmetries is insensitive to any variation in beam current that might be present between the two helicity states, a metric termed "charge asymmetry." However, as a precautionary measure, the charge asymmetry on the electron beam was minimized by fine tuning the Pockels cell voltages. Measured charge asymmetries were consistently small—typically below 10^{-3}—and are not used in further analysis.

Finally, we calculate the number of Mott triggers passing the TOF and energy cuts for the four detector arms, independent of helicity, for each scattering foil, normalized to the average beam current on the particular foil. These rates were corrected for both electronic dead time and DAQ dead time [42]. The average rate from the up and down detectors for run 1 and from left and right detectors for run 2 was used in the target thickness extrapolation. The details of the rate calculations and uncertainties are given in Ref. [45].

VIII. BEAM SYSTEMATICS

We have quantitatively examined a number of additional effects that might, in principle, affect our measured asymmetries. These include the reversal of the beam polarization effected by inserting a properly oriented half-wave plate before the Pockels cell, the temporal stability of the measured asymmetry during the target thickness extrapolation measurements that occurred over roughly a day of data taking, the motion of the beam spot on the target foil, variation in the beam spot size at the target foil, variations in the beam energy or energy spread, and the electronic dead time over the range of beam currents used.

A. Asymmetry dependence on laser polarization and wave-plate reversal

In setting up the laser system for the polarized source, we measured the circular polarization of the optical beam after the Pockels cell both with and without the half-wave plate, and for both Pockels cell voltages. Each of these four measurements gave a circular polarization of greater than 99.8%. These polarization numbers are very stable over extended periods of time (months).

Data from each scattering foil were accumulated in an even number of single Mott measurements of nominally equal integrated beam current—half with the insertable half-wave plate in, and half with the plate out. In run 1, the weighted average of the measured asymmetries with the wave plate out divided by that for the wave plate in was 1.0022 ± 0.0020, and in run 2 it was 1.0017 ± 0.0021. The primary effect of the half-wave plate is the reversal of the sense of circular polarization of the light illuminating the photocathode, and thus the beam polarization, while leaving all else nominally unchanged. The insertable half-wave plate essentially allows the elimination of any electronic pickup effect in the detector electronics associated with the reversal of the Pockels cell high voltage. While this is an important feature for parity-violation experiments where very small asymmetries are measured, with our very

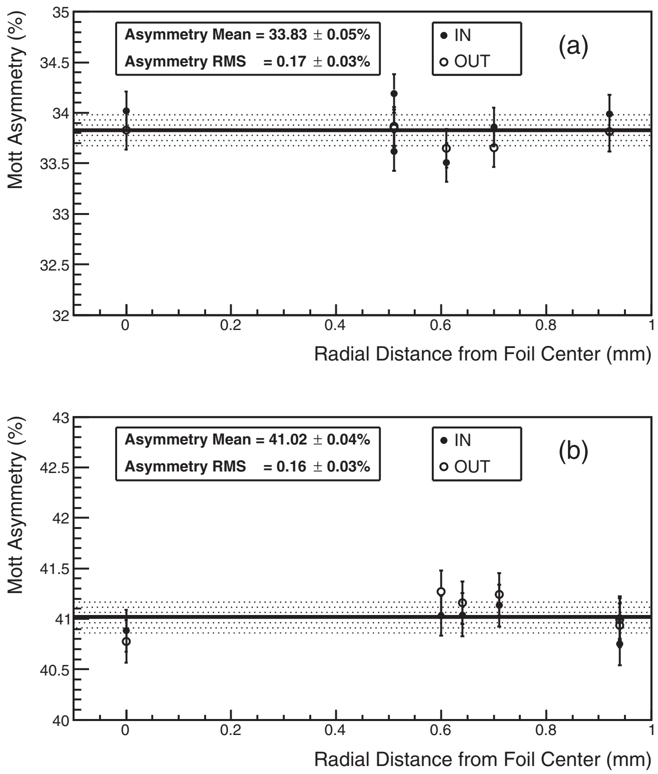

FIG. 14. Mott asymmetry vs radial displacement from the center of the target foil using the nominal (a) 1-μm and (b) 0.225-μm foils. The solid lines show the average value of all measured points, while the dotted region shows a $+/-$ 1σ band about this average.

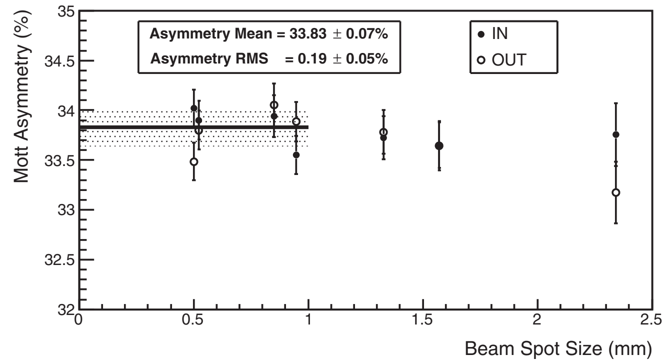

FIG. 15. Mott asymmetry vs beam size. The solid line shows the average value of all points with beam spot sizes no greater than 1.0-mm FWHM, while the dotted region shows a $+/-$ 1σ band about this average.

large asymmetries, the use of the wave plate is not expected to have any significant effect. We have made no correction to our physics asymmetry results for any difference between the wave plate out and wave plate in. In our data analysis, we treat the wave plate in and out asymmetries equally (with the appropriate sign). Overall, we estimate that the circular polarization of the optical beam is 0.998 ± 0.001. Since the Mott asymmetry is calculated using both helicities and any difference in polarization does not cancel in the cross-ratio method, a systematic uncertainty of 0.1% was assigned due to the different laser polarization between the $+$ and $-$ helicity states.

B. Asymmetry dependence on beam position and beam size at the scattering foil

We measured the scattering asymmetry as a function of beam position on the nominal 1- and 0.225-μm target foils during run 1. For each foil, we moved the beam to a total of six noncentered locations, spanning a radial distance of $\approx$1 mm from the foil center. The image position was verified by observing the beam spot with the OTR signal from the foil. The details are described in a JLAB technical note [46]. The results are consistent, within their statistical uncertainties, with all measured points representing the same value. The results are shown in Fig. 14. Realistically, any beam motion on the target foil is much smaller than the 1-mm displacements measured. This is the result of the high level of stabilization of all active beam line elements (magnets and rf cavities). Magnet currents and rf cavity amplitudes and phases are all controlled to a high degree by feedback stabilized power sources. The actual beam motion measured in the beam line to the Mott polarimeter, using microwave beam position monitors, is about 50-μm rms and the most likely source of beam motion is the effect of small stray ac magnetic fields in the low-energy region of the injector.

We also measured the asymmetry as a function of beam spot size (see Fig. 15), finding it to be independent for beam sizes less than 1-mm full width at half maximum (FWHM). Given the measured insensitivity of the asymmetry to beam steering, this result is expected.

C. Asymmetry dependence on beam energy, energy spread, scattering angle, and acceptance

The magnitude and stability of the beam energy and energy spread are determined almost exclusively by the rf phases and amplitudes of the two superconducting accelerating cavities. The remainder of the injector energy is determined by the 130-keV electron gun voltage (stability of $\approx 1 \times 10^{-4}$) and field strength of a normal conducting cavity, which provides $\approx$400 keV of energy gain. The amplitude and phase of the fields in all the rf cavities are controlled with precision rf control modules. For the superconducting cavities the cavity rf phase is controlled to less than 0.25° of the 1497-MHz phase over periods of days, and the amplitude is held to within 0.00045 rms of the set value [47] over a similar time period. These very tight tolerances assure that the beam energy and energy spread are stable during operation. Typical results are an energy spread of less than 4 keV in the 5-MeV region of the injector.

As was pointed out earlier, the beam kinetic energies were 4.806 ± 0.097 MeV for run 1, and 4.917 ± 0.013 MeV for run 2. The theoretical Sherman function at these energies (and a scattering angle of 172.6°, weighted by the Mott differential cross section and averaged over the 0.9° angular acceptance) is 0.514 ± 0.001 for both run 1 and run 2, resulting in a systematic uncertainty of 0.2%. The energy spread of the beam, other than being accounted for in the optical setup of

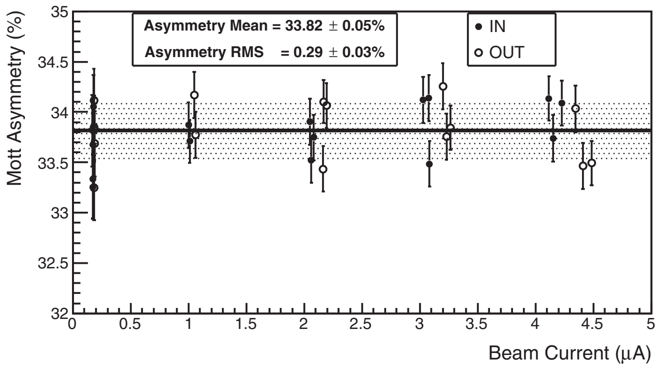

FIG. 16. Mott asymmetry vs beam current. The solid line shows the average of all measured points, while the dotted region shows a $+/-\ 1\sigma$ band about this average.

the beam spot size at the polarimeter target, is inconsequential to the scattering asymmetry.

D. Asymmetry dependence on electronic dead time

During run 1, we explored the effect of electronic dead time on our asymmetry measurements at five different average beam currents ranging from 0.245 to 4.3 μA incident on a 1-μm foil—the thickest foil used in our measurements—with dead time varying from 3 to 43% over this current range. All our measurements of asymmetry and counting rate versus target thickness were done with beam currents well within this range. The results are shown in Fig. 16. The five measurements are all within their statistical uncertainty of representing the same average value, a confirmation of the fact that common electronic dead time does not affect the asymmetry calculated with the cross-ratio method. We have thus made no correction to our physics asymmetry results for an electronic dead-time effect and no systematic uncertainty was assigned. On the other hand, a small correction to the counting rates in each detector arm was made, arising from the dead time associated with DAQ readout, as described in Ref. [45].

E. Dependence of asymmetry stability over time

During run 1 and run 2, we repeated the asymmetry measurement of the 1-μm foil after each target foil measurement, for a total of 42 measurements. In total, these measurements address the long term stability of the electron beam and Mott apparatus. The distribution of these repeated asymmetry measurements for run 1 and run 2 is shown in Fig. 17. Each measurement using the same 1-μm gold foil and a beam current of 1.0 μA yields a statistical uncertainty of about 0.21% in about 10 min. The rms width of these distributions is very close to the statistical accuracy of a single measurement. This shows that the relative contribution of the overall systematic uncertainty to any of the ten scattering asymmetries we measured for the target thickness extrapolation is negligible. It is notable that these measurements demonstrate the stability of both the electron beam and polarimeter over time scales longer than one day; specifically 26 h (run 1) and 27 h (run 2).

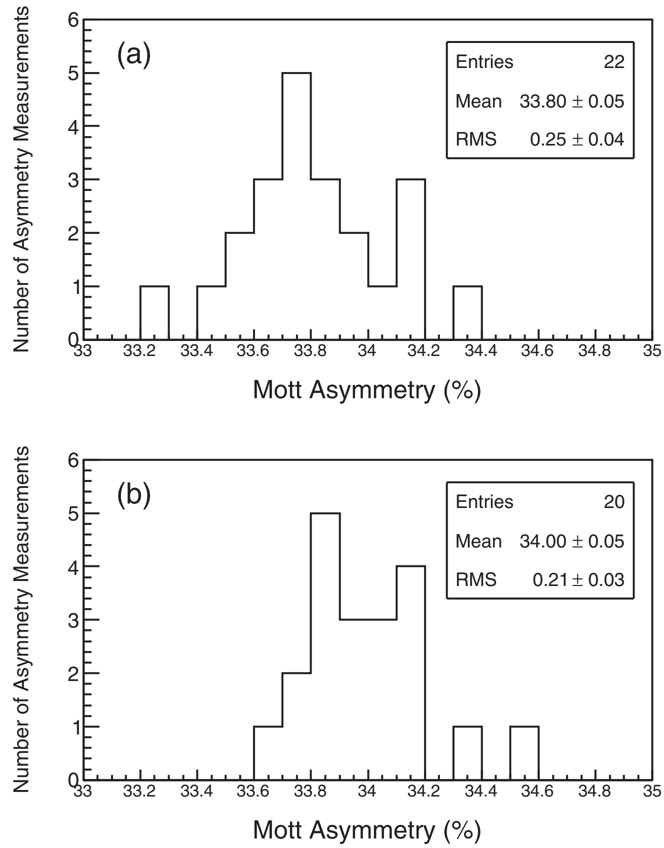

FIG. 17. Distribution of asymmetry values of the stability runs. (a) Stability measurements during run 1 (both low and high discriminator thresholds). (b) Stability measurements during run 2. The rms width of the distribution is very close to the statistical uncertainty of the single Mott measurement.

In summary, the effects we have examined indicate that any systematic uncertainties in our measured asymmetry are contributing a total of 0.24% to the measured beam polarization.

IX. TARGET THICKNESS EXTRAPOLATION

The Sherman function S is calculated for single elastic scattering from the nucleus, with corrections for the small effects due to the atomic electrons, as described in Sec. III. This value of S applies to an experiment with a zero-thickness target foil. To assign a beam polarization, an effective analyzing power that depends on target foil thickness must be determined from scattering asymmetries $A(t)$ measured for a range of target thicknesses t. The $A(t)$ measurements extrapolated to zero thickness $A(0)$ are used to assign the beam polarization by the relationship $P = A(0)/S(0) \equiv A(0)/S$. Once the value of the beam polarization is known the analyzing power of any foil, known as the effective Sherman function, may be determined from $S(t) = A(t)/P$.

Gold foils over a broad range of nominal thickness from 50 to 1000 nm were purchased from the Lebow Corporation. We independently measured the thickness of each foil using field emission scanning electron microscopy (FESEM). Although we refer to the foils by their respective nominal thickness as

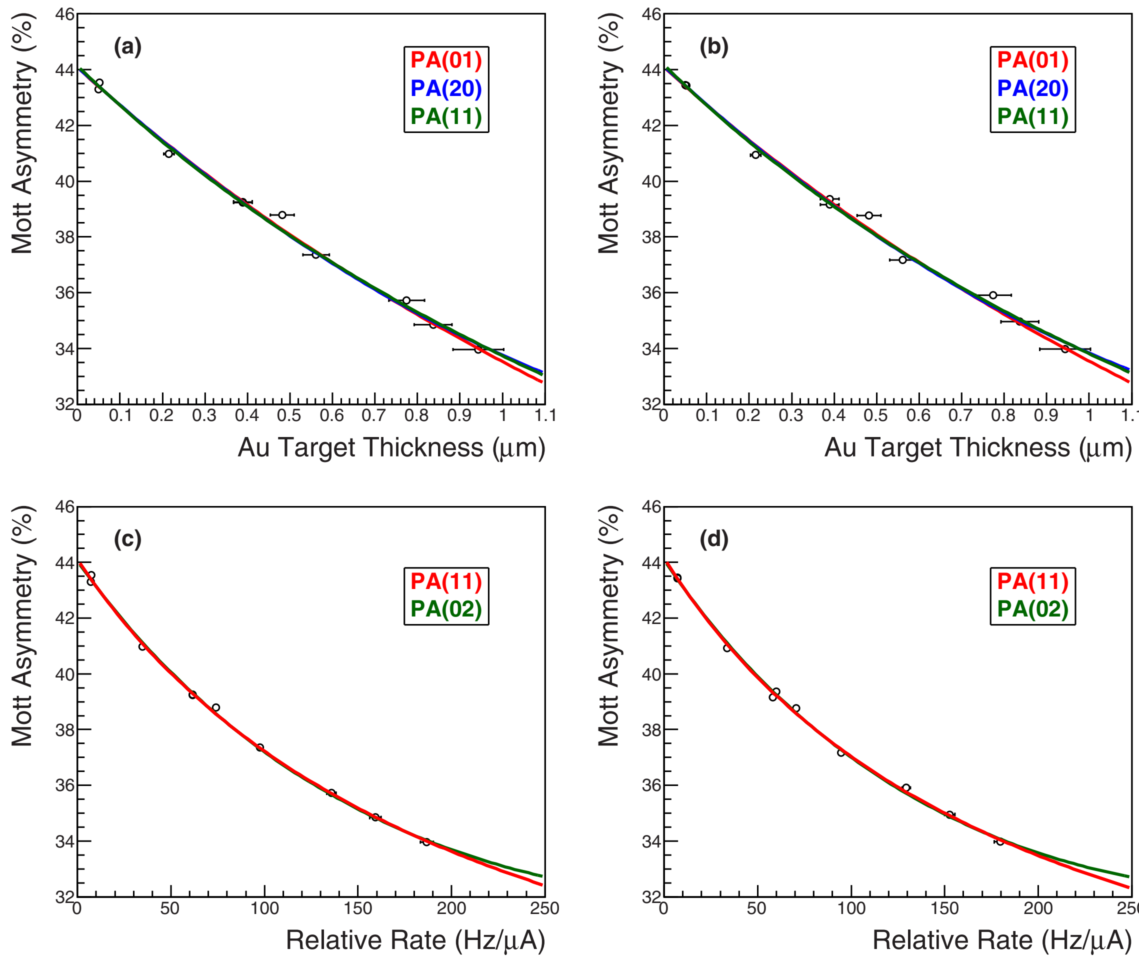

FIG. 18. Fits to the measured asymmetry vs foil thickness for run 1 (a) and run 2 (b), for the allowed Padé functions PA(01), PA(11), and PA(20), and for asymmetry vs relative rate for run 1 (c) and run 2 (d) and allowed Padé functions PA(11) and PA(02).

determined by the vendor, we use in our experimental analysis and theoretical models the values we determined by the FE-SEM method (summarized in the Appendix). The measured foil thicknesses are generally within 5% of those reported by the manufacturer. Measuring the scattering asymmetry for each foil thickness to high statistical precision (less than 0.25%) required from less than 1 h using the thickest foil to many hours for the thinnest. Only the statistical uncertainties of the measured asymmetries were included in the target thickness extrapolation. We could have included any of the relative systematic uncertainties but these were consistent with zero. The way we took the data on the different foils ensured no changes to the beam or polarimeter and the stability measurements taken during run 1 and run 2 show no relative systematic uncertainties (within the statistical precision).

Historically, and at lower energies less than 1 MeV (and typically 100–200 keV) where multiple and plural scatterings are more significant, the target thickness extrapolation has been performed by choosing one of a variety of empirical or model driven functional forms which lead to systematic uncertainties at the 1% level [9,48,49]. At higher energies, as is the case of this polarimeter, it is reasonable to assume that single and double scattering account essentially for all of the measured scattering asymmetry as the cross section falls as the energy is increased greater than 1 MeV.

The dependence of the analyzing power on the single and double scattering will affect the rate at which the scattering asymmetry falls with increasing target thickness. For example, in the case where there is no polarization dependence in the second scattering the asymmetry as a function of target thickness is of the form

$$\mathrm{A}(t) = A(0)/(1+\beta t).$$

If instead the second scattering also contributes an (albeit small) polarization dependence, the asymmetry as a function of target thickness becomes

$$\mathrm{A}(t) = A(0)[(1+\alpha t)/(1+\beta t)].$$

In this paper, rather than limiting the possible functions to those expected, we have systematized the $A(t)$ fitting procedure using the method of Padé approximants to determine those rational functions which best describe the data [50].

A Padé approximant is the quotient of two power series, which in our case are

$$A = A(0)\frac{(1 + a_1 t + a_2 t^2 + a_3 t^3 + \cdots\cdots + a_m t^m)}{1 + b_1 t + b_2 t^2 + b_3 t^3 + \cdots\cdots + b_n t^n}.$$

TABLE I. Fit parameters for zero foil thickness extrapolations vs either thickness or rate, including reduced χ^2 values.

	PA(mn)	a_0	a_1	a_2	b_1	b_2	Reduced $\chi 2$
Run 1 $A(t)$	PA(01)	44.06(10)			0.31(01)		1.2
	PA(20)	44.08(13)	−13.8(1.0)	3.5(1.2)			1.4
	PA(11)	44.12(14)	3.8(5.7)		0.41(16)		1.29
Run 2 $A(t)$	PA(01)	44.06(11)			0.31(01)		1.19
	PA(20)	44.10(14)	−14.0(1.0)	3.9(1.2)			1.35
	PA(11)	44.16(15)	5.7(5.9)		0.47(16)		1.23
Run 1 $A(R)$	PA(11)	44.09(11)	0.10(02)		$4.54(47) \times 10^{-3}$		1.34
	PA(02)	44.03(11)			$2.14(08) \times 10^{-3}$	$-3.03(47) \times 10^{-6}$	1.61
Run 2 $A(R)$	PA(11)	44.14(13)	0.12(02)		$5.03(55) \times 10^{-3}$		1.38
	PA(02)	44.07(13)			$2.26(10) \times 10^{-3}$	$-3.48(53) \times 10^{-6}$	1.69

In our analysis, we examined Padé approximants with m ranging from 1 to 3 and n ranging from 0 to 2, increasing the order of the fitting function until a statistical F test [51] indicates that larger values of m and/or n are not justified. The "F test" measures the impact of including additional higher-order Padé terms on the χ^2 value of the resulting fit. All fits that passed the F test were then judged by their reduced χ^2. Reduced χ^2 values larger than 2 indicate a less than 2% likelihood of accurately representing the data, and lead to the rejection of the associated PA(m,n).

Plots showing the allowed Padé solutions of both $A(t)$ for the two experimental runs are shown in Figs. 18(a) and 18(b), followed by a table giving the Padé function parameters and the reduced χ^2 values for the fits to the data.

Alternatively, one can also consider the measured asymmetry A as a function of the relative rate, R, averaged from both detectors, corrected for dead time, and normalized to the measured beam current [52]. The advantage of doing this is that the number of counts is very large, and thus should generally lead to fits with smaller statistical uncertainty. The total uncertainty on the relative rate was about 2% and is a combination of the statistical uncertainty and systematic uncertainties due to the beam current measurement and dead-time correction.

Plots showing the allowed Padé solutions of both $A(R)$ for the two experimental runs are shown in Figs. 18(c) and 18(d) and the fit results are shown in Table I. The values for $A(R)$ at $R = 0$ and $A(t)$ at $t = 0$ are essentially equal within a small fraction of their fit uncertainty.

Use of Padé approximants, the F test, and the reduced χ^2 test indicates the best fits in both runs are to the $A(t)$ data and by the function PA(01). It is noteworthy that PA(01) and the next best fit PA(11) are the two functions described above that reflect the expected contributions of both single and double scattering in the measured scattering asymmetry.

The $A(0)$ results of all of the successful Padé functions presented in Table I are graphically represented in Fig. 19. That all are in good agreement to well within 1 σ demonstrates the challenge that remains to *a priori* analytically forecast the only correct function. However, based on the statistical analysis discussed above we can argue the best fit to our data is the $A(t)$ function PA(01), giving 44.06(10) for run 1 and 44.06(11) for run 2, and a corresponding relative uncertainty of 0.25% in the determination of $A(0)$.

From an examination of the fits to the four groups of data listed in Fig. 18, the data points for the 482- and 215-nm target foils are the largest outliers from the fit. We thus examined fits to the normalized counting rate versus the foil thickness to check for anomalies. These fits were forced through $R(0) = 0$ at $t = 0$, and can be compared to the GEANT4 simulations discussed in the next section. The data for rate versus thickness are plotted in Fig. 20, with coefficients in Table II; the fits are very good, and no anomalies are apparent.

Finally, using the values of $A(0)$ and $dA(0)$ determined from run 1 and run 2, divided by the Sherman function of 0.514 calculated in Sec. VIII, gives beam polarizations of 85.72 ± 0.19% for run 1 and 85.72 ± 0.21% for run 2. It is interesting to note that these very similar results are from two

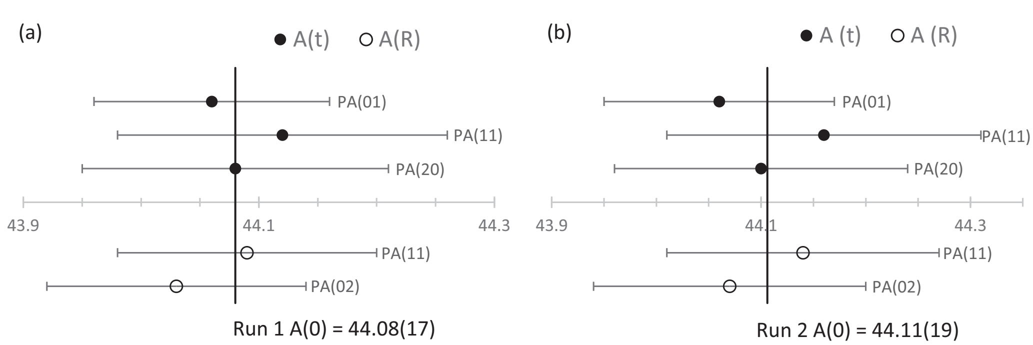

FIG. 19. The values of $A(0)$ extrapolated from thickness (solid dots) or rate (open circles) using the Padé approximants are shown for (a) run 1 and (b) run 2. The solid vertical line is the average (unweighted) of the $A(0)$ fit parameters.

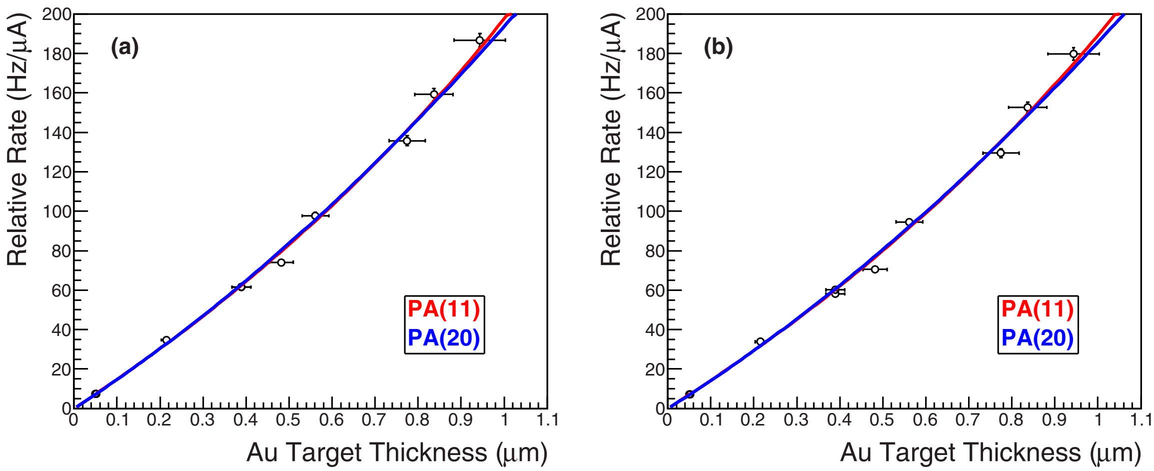

FIG. 20. Normalized counting rate vs foil thickness for (a) run 1 and (b) run 2.

different photocathodes cut from a single wafer, indicating the excellent uniformity of the growth of this complex semiconductor structure.

X. GEANT4 SIMULATION OF THE POLARIMETER

A GEANT4 [53] model of the polarimeter was constructed to simulate the scattering rate and asymmetry as a function of target thickness, motivated by Wegener's argument [23] which concludes that single and double scattering essentially account for all of the observed dependence of the analyzing power on target thickness. Further, we anticipate that our data can be well simulated with this model, which is strongly supported both by our Padé approximant analysis of our asymmetry measurements and for our energy range by the results of the Mainz experiment [15].

Clearly, single scattering will have a counting rate proportional to the scattering foil thickness, and an asymmetry independent of the foil thickness, while the double-scattering rate will depend on the square of the foil thickness, and also have an asymmetry independent of the foil thickness. Thus we can write the scattering rate into the left (L) and right (R) detectors (or up and down detectors) for a beam of polarization $\mathbf{P} = P_0\mathbf{y}$ as a function of the foil thickness t:

$$R_{\mathrm{L1}} = a_1{}^{\mathrm{sim}} t(1 + P\varepsilon_1), \quad R_{\mathrm{R1}} = a_1{}^{\mathrm{sim}} t(1 - P\varepsilon_1),$$
$$R_{\mathrm{L2}} = a_2{}^{\mathrm{sim}} t^2(1 + P\varepsilon_2), \quad \text{and } R_{\mathrm{R2}} = a_2{}^{\mathrm{sim}} t^2(1 - P\varepsilon_2),$$

where the subscripts 1 (2) refer to single (double) scattering, and the a and ε parameters are the simulated scattering rates and analyzing power coefficients for the two processes. Using the common definitions for the measured scattering rate and asymmetry, one finds

$$R_{\mathrm{tot}}{}^{\mathrm{sim}} = 1/2[R_{\mathrm{L1}} + R_{\mathrm{R1}} + R_{\mathrm{L2}} + R_{\mathrm{R2}}],$$

and

$$A^{\mathrm{sim}} = ([R_{\mathrm{L1}} - R_{\mathrm{R1}}] + [R_{\mathrm{L2}} - R_{\mathrm{R2}}])/ ([R_{\mathrm{L1}} + R_{\mathrm{R1}} + R_{\mathrm{L2}} + R_{\mathrm{R2}}]).$$

These lead to expressions for the predicted scattering rate and asymmetry:

$$R^{\mathrm{pred}}(t) = a_1 t + a_2 t^2$$

and

$$A^{\mathrm{pred}}(t) = P(a_1\varepsilon_1 + a_2\varepsilon_2 t)/(a_1 + a_2 t).$$

Using only quantities derived from our simulations, the predicted effective Sherman function is

$$S^{\mathrm{pred}}(t) = (a_1\varepsilon_1 + a_2\varepsilon_2 t)/(a_1 + a_2 t).$$

In our simulations of the polarimeter, the relevant geometry and material properties of the detector package and scattering chamber were used. The theoretically calculated values of the cross section ($d\sigma/d\Omega$), Sherman function (S), and spin-transfer functions (T, U) as defined in Ref. [10] were also used. Aside from these terms, the GEANT4 electromagnetic physics package was used. The initial electron distribution was defined with momenta in the longitudinal direction ($\mathbf{p} = p_0\mathbf{z}$), and polarization in the vertical direction ($\mathbf{P} = P_0\mathbf{y}$). The electron beam at the target foil was defined as a transverse

TABLE II. Rate vs thickness fits for runs 1 and 2.

		a_0	a_1	a_2	b_1	Reduced $\chi 2$
Run 1 R(t)	PA(11)	0	143.42(3.62)		−0.27(0.04)	0.39
	PA(20)	0	141.37(4.57)	51.42(8.76)		0.34
Run 2 R(t)	PA(11)	0	138.70(4.27)		−0.26(0.04)	0.50
	PA(20)	0	136.91(5.24)	47.54(9.98)		0.55

Gaussian of 1-mm FWHM diameter and with a mean energy of 4.9 MeV and Gaussian energy spread of 150-keV FWHM. Although the measured values of the energy spread (≈4 keV) are considerably smaller, we chose larger and more conservative values in the simulation. Experimentally, we find both the measured scattering rates and calculated asymmetries to be insensitive to values less than those used in the GEANT4 simulation.

We used the method of rejection sampling [54] to determine the values for the asymmetries ε_1 and ε_2 from single and double scattering. In the single-scattering case, we used the following algorithm.

(1) Choose a scattering position $\mathbf{x_1}$ within the intersection of the beam and our scattering foil.
(2) Choose a point $\mathbf{x_2}$ within the acceptance of the primary collimator.
(3) Calculate $d\sigma/d\Omega(\mathbf{x_1}, \mathbf{x_2})$.
(4) Rejection sample this value of $(\mathbf{x_1}, \mathbf{x_2})$ against the calculated cross section. If accepted generate the event. If rejected, repeat the first three steps.

Implementing these steps in the simulation, the single-scattering parameter is

$$\varepsilon_1 = (N_{\mathrm{L1}} - N_{\mathrm{R1}})/(N_{\mathrm{L1}} + N_{\mathrm{R1}}) = -0.513 \pm 0.001,$$

in excellent agreement with the theoretical value of the single-atom scattering asymmetry of -0.514 ± 0.003 described in Sec. III, which provides important validation of the simulation algorithm.

For the case of double scattering, we used the following algorithm.

(1) Choose a scattering position $\mathbf{x_1}$ within the intersection of the beam and our scattering foil.
(2) Choose a point $\mathbf{x_2}$ within the foil such that $|\mathbf{x_2} - \mathbf{x_1}| < 0.16$ mm. Beyond this distance an electron would have lost sufficient energy to fall outside of our cuts.
(3) Calculate $d\sigma_1/d\Omega_1(\mathbf{x_1}, \mathbf{x_2})$.
(4) Choose a point $\mathbf{x_3}$ within the acceptance of the primary collimator.
(5) Calculate $d\sigma_2/d\Omega_2(\mathbf{x_2}, \mathbf{x_3})$.
(6) Rejection sample this value against $(d\sigma_1/d\Omega_1)(d\sigma_2/d\Omega_2)$. If accepted generate an electron at $\mathbf{x_2}$ towards $\mathbf{x_3}$. If rejected repeat the first five steps.

Simulation of 10^7 events at each foil thickness produces an asymmetry of

$$\varepsilon_2 = (N_{\mathrm{L2}} - N_{\mathrm{R2}})/(N_{\mathrm{L2}} + N_{\mathrm{R2}}) = -0.011 \pm 0.003.$$

The double-scattering simulation results for one detector are shown in Fig. 21. As anticipated, these results clearly show that the first scattering is in or exceptionally close to the plane of the foil, while the second scattering shows significant peaks at $90^\circ \pm 7.4^\circ$ to produce the required total scattering angle of 172.6° for electrons to arrive at the detectors.

The rate coefficient for single scattering into the four detector channels was computed by a numerical integration over the initial parent phase space $(x, y, z, E, \theta, \phi)$ without regard to the electron polarization. The result for the total single-scattering rate coefficient is

$$a_1{}^{\mathrm{sim}} = 198 \pm 1\,\mathrm{Hz}/(\mu\mathrm{A} - \mu\mathrm{m}).$$

Such an integration cannot be used to calculate the double-scattering rate coefficient, as the phase space is significantly more complex, and the integration must be performed over more dimensions. Instead, a numerical Monte Carlo estimator was used to uniformly sample and integrate from the phase space of double-scattering events originating from the target foil and reaching the detector acceptance. The distance between the first and second scattering in the foil was restricted to be less than 160 μm, corresponding to the distance in which an electron would lose 500 keV and thus fall outside the energy cuts we used. In practice, this cut did not have a significant impact on the result. Our result for the total double-scattering rate coefficient is

$$a_2{}^{\mathrm{sim}} = 62 \pm 15\,\mathrm{Hz}/(\mu\mathrm{A} - \mu\mathrm{m}^2).$$

With simulation results in hand for both the single- and double-scattering rates and asymmetries, we can compare with actual data, shown in Figs. 22(a)–22(d). In order to make a comparison between GEANT4 simulations with experimental results it is necessary to relieve the stringent energy cuts that are applied in the experimental data reduction (see Figs. 11 and 12) which throw out some fraction of good events. While less important for the computed asymmetry, this is especially necessary when comparing the calculated simulation rate with a corresponding experimentally measured rate.

The simulated asymmetries, which are insensitive to these details, are in quite good agreement with the measured asymmetries. Although there is some variation between the simulated and experimental counting rates, these very likely arise from our estimation of the total counting rate, with large uncertainty in the estimation of a background subtraction which was made of the E detector spectrum corresponding to otherwise good simulated events that were well outside of the stringent energy cuts that we applied in Secs. VI–IX. Overall, we conclude that the GEANT4 simulation of the polarimeter gives quite a good description of its performance.

XI. CONCLUSIONS AND FUTURE PLANS

The primary conclusion from our measurements and analysis is that electron polarimetry based on Mott scattering in the few-MeV range has reached a level we believe is well below 1% uncertainty.

Our polarimeter design is optimized to isolate electrons which only scatter from the target foil. The use of a coincidence ΔE-E detector and measurement of both the energy and timing of the scattered electrons allows for careful isolation of elastic events that carry the full asymmetry of the analyzed beam. The use of the super-ratio method makes the computed asymmetry insensitive to beam intensity and detector solid angles. Systematic studies of the DAQ and of dependence on the meaningful beam properties demonstrate these effects contribute less than 0.24% to the measured asymmetry.

The target thickness extrapolation, a questionable uncertainty owing to the challenges associated with knowledge of

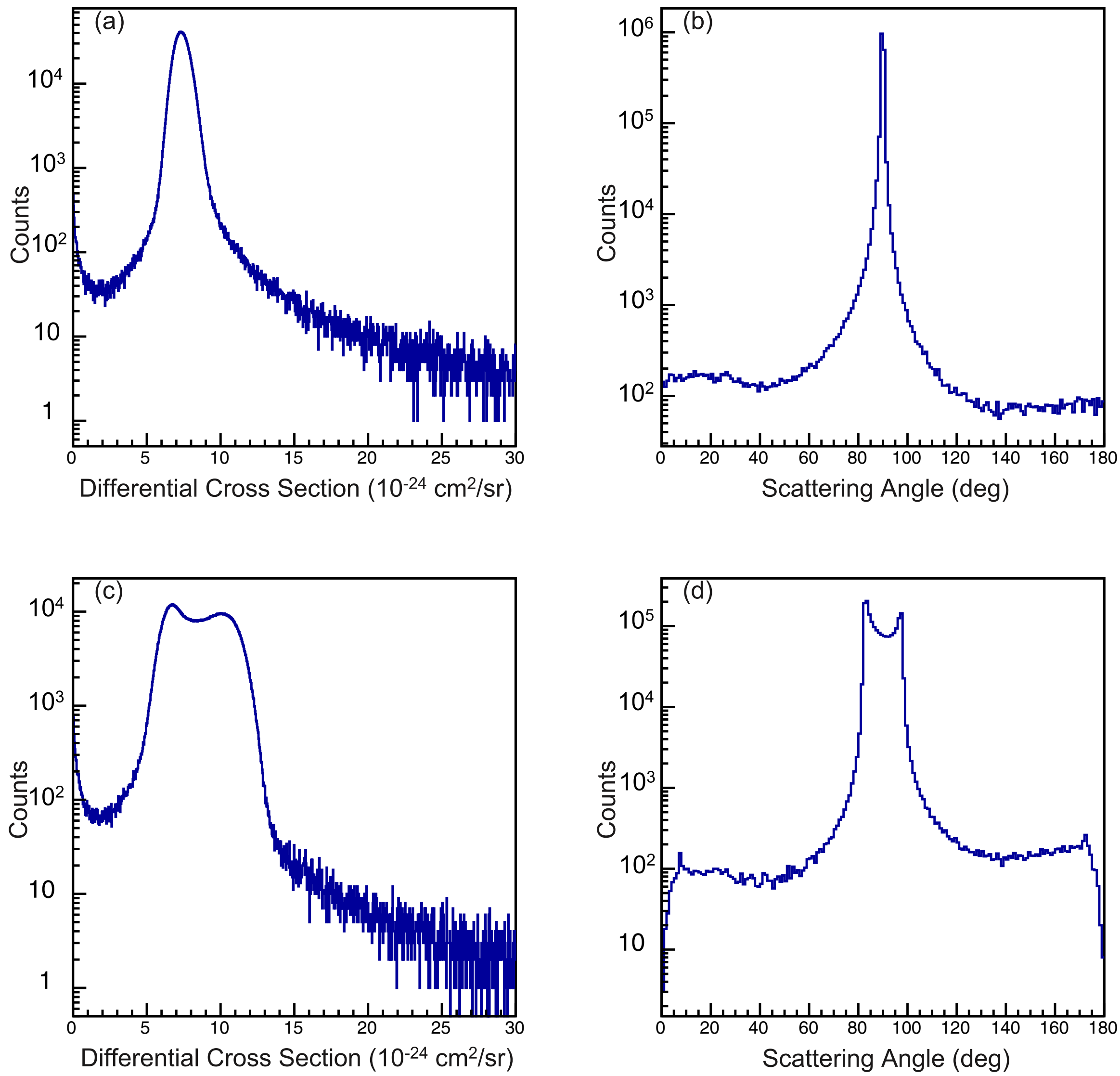

FIG. 21. The results for the simulation of double-scattering events into one detector arm show the (a) cross section and (b) scattering angle of the first scattering within the plane of the target foil and the (c) cross section and (d) scattering angle for the second scattering towards the Mott detector. The phi angle was also simulated, but does not alter the simulation results above.

the physical dependence, has been especially well characterized in this paper. Extensive measurements and statistical analysis have demonstrated knowledge of the zero-thickness foil analyzing power with a precision of $\approx$0.25%. While the calculation of the theoretical Sherman function remains the large contribution to the absolute uncertainty the modern calculations presented here predict this value convincingly at a level of $\approx$0.5%. Consequently, we have demonstrated the capability to measure the electron polarization at a beam energy with a total uncertainty $\approx$0.6% (see Table III).

The statistical precision of measured scattering asymmetry for each target foil was about 0.25% and can easily be improved beyond this level in practical periods of time or by operation at higher beam current. A GEANT4 model was developed that predicts the dependence of the analyzing power on target foil thickness in good agreement with our measurements. While the fact that the leading-order QED corrections and the real bremsstrahlung correction are not fully calculated at MeV energies is displeasing, it is also true that these small corrections all show a significant dependence on both energy and Z, allowing meaningful bounds on the total contribution of these terms to be experimentally established. The vacuum polarization and real bremsstrahlung corrections appear to be of the same sign, and there is good reason to believe that the self-energy correction is of the opposite sign, thus offering some degree of cancellation. Two previous measurements, each covering a significant and different range in energy and using very different polarimeters, have made no correction for the sum of these effects, and yet showed agreement well below the 1% level over the energy ranges measured. We have made initial asymmetry measurements at three different Z values (29, 47, and 79) and at energies between 2.75 and 8.2 MeV. These measurements can be done with much greater precision, and a serious study of the Z and energy dependence of the analyzing power should readily yield meaningful limits on the total of these small corrections. It would also be useful to

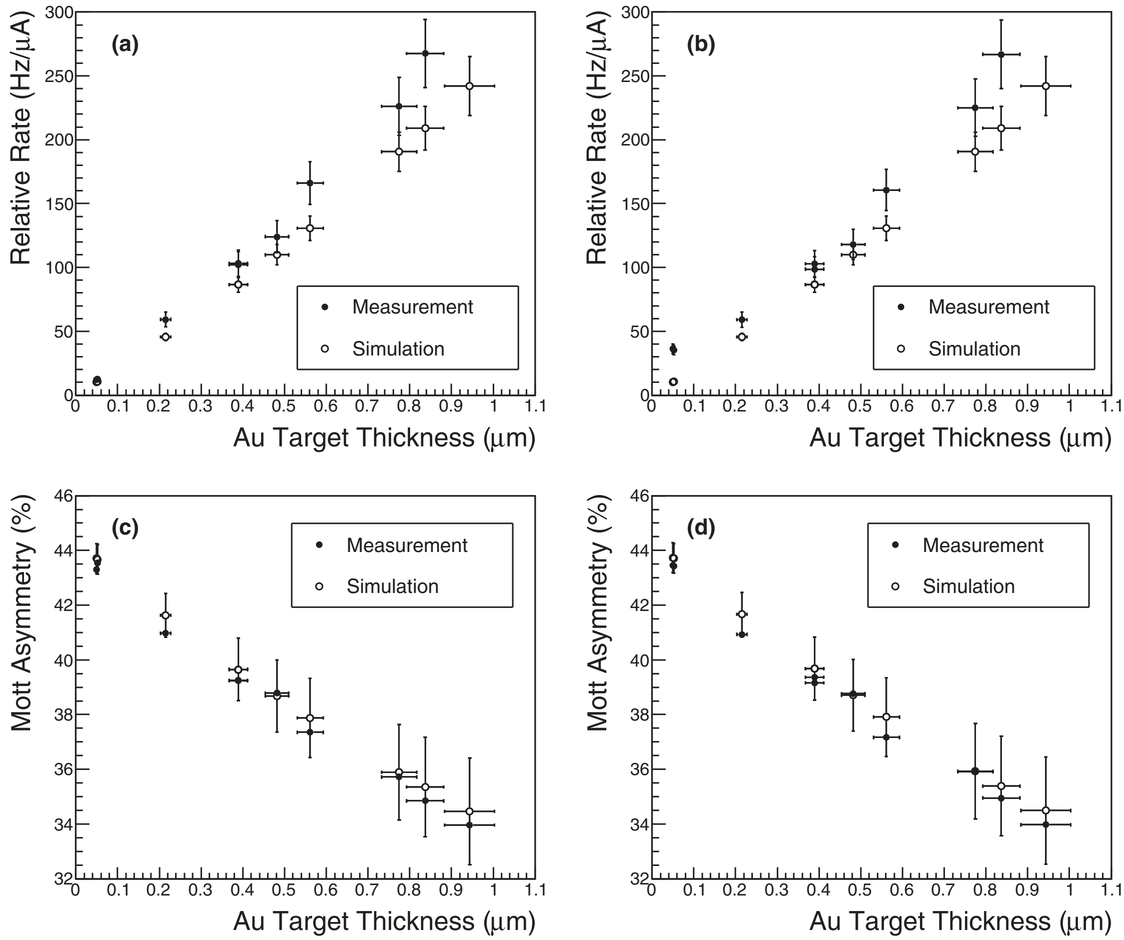

FIG. 22. Measured counting rates compared to the GEANT4 simulation for (a) run 1 (U/D) and (b) run 2 (L/R), and the measured asymmetry for (c) run 1 and (d) run 2, all vs FESEM measured foil thickness.

extend the bremsstrahlung calculations of Johnson *et al.* [33] to our kinematic region.

As strong and as well supported as the above statements are, no one would accept the precision claimed for this Mott polarimeter without clear and independent corroboration. This may be had by comparing measurements of the electron polarization obtained by independent polarimetry techniques. In 2000, this was first done at the $\approx 2\%$ level for the five polarimeters at Jefferson Lab [25]. These measurements are made possible by the fact that polarization placed in the horizontal plane in the injector remains in the horizontal plane after passage through the full multipass CEBAF accelerator permitting measurement of the beam polarization at both the injection energy and high energy by simply sweeping the polarization through 180° in the horizontal plane at the injector. These first measurements clearly demonstrated that the claimed analyzing powers for the various polarimeters were not in agreement at the 1–2% level, and that one polarimeter was in more serious disagreement. Since that time all the high-energy polarimeters have been upgraded [48,55–58] and have improved their systematic and statistical precision. Moreover, an additional Compton polarimeter has been installed in hall C. Thus we are at a point where another multipolarimeter comparison, at the 0.5% or better level, is warranted. This statement is supported by a recent review of precision electron polarimetry which demonstrates that Mϕller polarimeters now reach precisions of 0.8 to 0.9% while Compton polarimeters reach $\approx 0.6\%$ uncertainties at few-GeV energies [48].

A different approach involves making an absolute measurement of the electron-beam polarization from the same photocathode and laser illumination system used for the Mott polarization measurements. This is made possible by the fact that the photocathode used in the CEBAF injector can be re-

TABLE III. Uncertainty budget for the 5 MeV Mott polarimeter.

Contribution to the total uncertainty	Value
Theoretical Sherman function	0.50%
Target thickness extrapolation	0.25%
Systematic uncertainties	0.24%
Energy cut (0.10%)	
Laser polarization (0.10%)	
Scattering angle and beam energy (0.20%)	
Total	0.61%

moved from the electron gun and transported under ultrahigh vacuum to an optical polarimeter, AESOP (Accurate Electron Spin Optical Polarimeter). The AESOP method is being developed at the University of Nebraska in collaboration with Jefferson Lab [59,60]. In this method, a polarized electron excites a noble gas atom to a triplet state by spin exchange. The polarization of the light emitted along the axis of the initial electron-spin polarization in the decay of the atom to a lower triplet level is observed. The spin orientation of the incident electron results in the partial circular polarization of the decay photon through spin-orbit coupling in the excited atomic state. If the excited atomic state is well L-S coupled, the circular polarization can be directly related to the electron polarization without the need for dynamical calculations. The measurement of the Stokes parameters of the decay radiation thus provides an absolute calibration standard for electron polarization. While this method relies on a high-precision measurement of the Stokes parameters of the decay photon, it appears possible to make an electron polarization measurement with an absolute precision of $\approx 0.5\%$ by this technique.

There are changes to the present polarimeter that could deliver meaningful reductions in the uncertainty of the measured polarization. Redesigning the detector package for better light collection could significantly reduce the width of the elastic peak in the energy spectrum, resulting in smaller and less uncertain cuts in separating the elastic-scattering events from the lower-energy background. It is worth considering replacement of the plastic scintillator of the E detector with a higher-quality crystalline scintillator. A higher-density scintillator would allow a reduction in its physical size, which would give some reduction in E detector backgrounds, but simulations to validate this idea are necessary. It is also practical to reduce the transverse size of the ΔE detector, and possibly its thickness, again reducing background counts. These changes would also prove helpful in operation with higher beam currents.

Operation at higher beam currents would be useful in obtaining even-higher-precision polarization measurements. The introduction of a beryllium beam dump was helpful to reduce background counting rates. The use of a relatively thin Be liner inside the beam pipe leading to the beam dump might be prohibitively costly, but would likely result in further background reduction. A portion of the beam dump tube closest to the dump plate could be enlarged, and the dump plate could be moved further from the detectors. These changes can be explored in simulations before implementing them, but it seems clear that improvements are practical.

Changing the length of the beam dump tube would also be beneficial. We made an unfortunate choice of the length of the beam dump tube, as it places the dump plate 12 ns away from the scattering foil, while the beam pulse repetition rate is an integer multiple of 2 ns. The concern is that electrons originating from an earlier 499-MHz beam pulse reflecting from the dump plate may arrive at the target foil in time with a new beam pulse reaching the target foil. However, in analyzing our data collected with a 31.1875-MHz beam pulse repetition rate, meaning a pulse spacing longer than the dump plate spacing, we observed that the addition of TOF analysis made only a small improvement, and only in the case of the thinnest target foils. This is because with all but the thinnest of foils the background events that arrive at the target foil are likely to have had inelastic energy losses from multiple surfaces and be removed through energy cuts. Thus, this polarimeter calibration, despite the fact that it was done at 32 MHz, is still applicable to 499 MHz when the 1-μm foil is used. With a nominal electron-beam kinetic energy of 4.9 MeV, the effective Sherman function for the 1-μm foil is 0.3921.

Moving the dump plate an additional 15 cm further from the scattering foil would not totally eliminate this background, but would very substantially reduce it. Some combination of enlarging the beam dump tube for a fraction of its length closest to the dump plate (with the addition of appropriate shielding), moving the dump plate an odd integer multiple of 15 cm further away from the scattering foil, and to the extent feasible adding Be liners to the dump tube would give a very significant reduction in the backgrounds.

Finally, some small additional improvements may come from improved knowledge of the thickness of the different scattering foils. The foils for the Mainz polarimeter reported in Ref. [24] were measured by α scattering, with a claimed precision of $\approx 3\%$. This is considerably better than the foil thickness uncertainty we measured by the FESEM technique ($\approx 5\%$), which in turn was a real improvement on the original thickness uncertainty quoted by the manufacturer of $\approx 10\%$.

In conclusion, we have been able to demonstrate a meaningful improvement in the uncertainty of the electron-beam polarization measured by few-MeV Mott scattering, to an accuracy $\approx 0.6\%$. The dominant uncertainty in our result arises from the imperfect knowledge of the Sherman function. The uncertainty in the Sherman function calculations and the uncertainty in the experimental measurement of the asymmetry and the extrapolation to zero thickness provide similar contributions to the accuracy of the measurement. The higher-order effects in the Sherman function calculation can be constrained. We have the capability to reduce this uncertainty significantly by measurements over a range of energies and from different Z scattering foils, and the experimental uncertainty can be improved with increased statistics and improved target thickness characterization. We believe that an overall uncertainty of electron polarization measurement below 0.5% will prove practical in the future. The possibility of making a separate, absolute measurement of the polarization from the photocathode and laser system used for beam generation with an AESOP polarimeter is being pursued. Moderate improvements to the scattering chamber downstream of the scattering foil will likely allow precision polarization measurement at much increased beam current. And, lastly, a new and improved precision comparison of the polarization measured by all the various polarimeters at Jefferson Lab seems important to the ultimate goal of demonstrating polarization measurement at or below the 0.5% level accuracy desired by the next generation of parity-violation measurements.

ACKNOWLEDGMENTS

This paper was authored by Jefferson Science Associates under U.S. Department of Energy Contract No. DE-AC05-

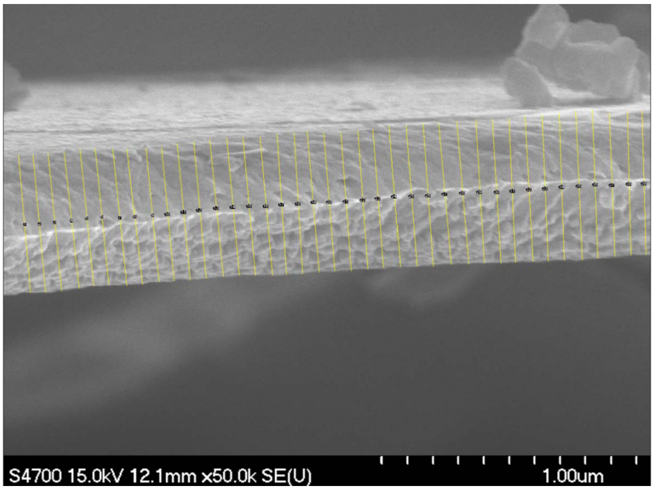

FIG. 23. FESEM image of a nominal 625-nm-thick gold foil mounted on a silicon substrate (lower dark region). Many measurements of the thickness along this region indicate the foil is 561.2 ± 31.0 nm. Yellow lines with black labels denote the lines used for thickness analysis with ImageJ software [62].

84ER40150. The U.S. Government retains a non-exclusive, paid-up, irrevocable, worldwide license to publish or reproduce this manuscript for U.S. Government purposes. This work has also been funded in part by the NSF under (T.J.G.) Grants No. PHY1505794, No. PHY1632778, and No. PHY1806771. X.R.-M. acknowledges funding from the European Union's Horizon 2020 research and innovation program under Grant No. 654002. We acknowledge the important early contributions of M. Steigerwald, P. M. Hartmann, P. Rutt, J. S. Price, D. Mack, K. Assamagan, and B. Wojtsekhowski. D. Machie, P. Adderley, A. Day, K. Ryan, and J. Clark provided excellent technical support for the design and installation of the polarimeter, and the many changes made spanning more than 20 years.

APPENDIX: THICKNESS MEASUREMENTS OF THE GOLD TARGET FOILS

Ten freestanding gold foils of varied thicknesses were mounted on the target ladder and used for this experiment. The 50-nm foils were constructed using a 50-μm Kapton sheet with a 10-mm-diameter aperture that supported the freestanding gold target foil. The other foils were all freestanding gold over a 25.4-mm-diameter circular aperture. All foils were manufactured by the Lebow Corporation from 99.99% pure gold. While Lebow does not measure the absolute thickness of the foils as delivered, they are guaranteed to be within 10% of the specified thickness, and uniform to 2% over the active area of the foil. Foils of a given thickness manufactured in a single batch (called "siblings") are guaranteed to have the same thickness to within 5%.

To obtain more accurate foil thickness values, we conducted a series of measurements using FESEM [61]. The very high brightness of a field emission electron source makes it possible to obtain images with nanometer level precision. We used a Hitachi s-4700 FESEM at 15 kV. Magnifications between 10 000 and 150 000 were used depending on the foil thickness being measured. For the measurements, sibling foils of those used for the Mott measurements were mounted on a silicon substrate which was subsequently cleaved to expose a cross section of the foil. Although we believe this foil preparation process does not meaningfully change the apparent foil thickness at the location of the cleavage, we have not conducted detailed studies to verify this. A typical FESEM picture showing a gold foil on a silicon substrate is shown in Fig. 23.

The determination of the foil thickness from the FESEM pictures was done with ImageJ software [62]. Generally, FESEM images were made at a single location for each sample. The random uncertainty in the measurements was determined by measuring a number of different images of the same foil at the same position. Since these measurements should be identical, the variation is a good measure of the statistical uncertainty in the technique.

Systematic uncertainties arise from the inherent resolution of the FESEM, from the variation in measured thickness in multiple analyses of the same image, and from the 5% possible variation between the sibling foil measured and the actual foil used in the Mott measurement. The largest of these is the uniformity of sibling foils; since the thickness measurement is a destructive testing technique and we cannot measure the samples on the target ladder, this sibling uncertainty dominates the overall uncertainty for all but the 50-nm (thinnest) foil. The vendor and FESEM thickness and total uncertainty for each foils followed by the statistical image analysis uncertainty and the three contributions to systematic uncertainty are shown in Table IV.

TABLE IV. Summary of purchased target foils and their FESEM measured thicknesses and corresponding uncertainty.

Lebow thickness (nm)	1000	870	750	625	500	355	225	50
FESEM thickness (nm)	943.7	836.8	774.5	561.2	482.0	389.4	215.2	52.0
FESEM uncertainty (nm)	59.8	44.2	41.9	31.0	27.7	22.1	11.7	4.7
Image analysis (nm)	29.0	7.1	9.1	8.0	9.7	4.5	1.9	2.3
FESEM resolution (nm)	1.2	1.2	1.2	1.2	1.2	1.2	1.2	1.2
Same image reanalysis (nm)	22.6	12.4	13.3	10.2	9.7	9.2	3.8	2.9
Lebow sibling 5% (nm)	47.2	41.8	38.7	28.2	24.1	19.5	10.8	2.6

[1] N. F. Mott, The scattering of fast electrons by atomic nuclei, Proc. R. Soc. A **124**, 425 (1929).
[2] W. A. McKinley and H. Feshbach, The Coulomb scattering of relativistic electrons by nuclei, Phys. Rev. **74**, 1759 (1949).
[3] J. A. Doggett and L. V. Spencer, Elastic scattering of electrons and positrons by point nuclei, Phys. Rev. **103**, 1597 (1956).
[4] N. Sherman, Coulomb scattering of relativistic electrons by point nuclei, Phys. Rev. **103**, 1601 (1956).
[5] C. G. Shull, C. T. Chase, and F. E. Myers, Electron polarization, Phys. Rev. **63**, 29 (1943).
[6] W. H. Louisell, R. W. Pidd, and H. R. Crane, An experimental measurement of the gyromagnetic ratio of the free electron, Phys. Rev. **94**, 7 (1954).
[7] A. R. Brosi *et al.*, A Precision measurement of the longitudinal polarization of betas following ^{32}P decay, Nucl. Phys. **33**, 353 (1962).
[8] J. S. Greenberg, D. P. Malone, R. L. Gluckstern, and V. W. Hughes, Mott-scattering analysis of longitudinal polarization of electrons from Co^{60}, Phys. Rev. **120**, 1393 (1960).
[9] T. J. Gay and F. B. Dunning, Mott electron polarimetry, Rev. Sci. Instrum. **63**, 1635 (1992).
[10] J. Kessler, *Polarized Electrons*, 2nd ed. (Springer-Verlag, Berlin, 1985).
[11] C. K. Sinclair, The development of polarized electron sources: Physics and history, in *12th International Workshop on Polarized Ion Sources, Targets and Polarimetry - PSTP2007*, edited by A. Kponou, Y. Makdisi, and A. Zelenski, AIP, Conf. Proc. No. 980 (AIP, Woodbury, NY, 2008), p. 25.
[12] M. Allet *et al.*, Search for Time-Reversal Violation in the Beta Decay of ^{8}Li, Phys. Rev. Lett. **68**, 572 (1992).
[13] J. Sromicki *et al.*, Study of time reversal violation in β decay of polarized ^{8}Li, Phys. Rev. C **53**, 932 (1996).
[14] D. Conti *et al.*, Mott scattering of multi-MeV electrons from heavy nuclei, in *Proceedings of the Seventh International Workshop on Polarized Gas Targets and Polarized Beams*, edited by R. J. Holt and M. A. Miller, AIP Conf. Proc. No. 421 (AIP, Woodbury, NY, 1998), p. 326.
[15] J. Sromicki *et al.*, Polarization in Mott Scattering of Multi-Mev Electrons in Heavy Nuclei, Phys. Rev. Lett. **82**, 57 (1999).
[16] P. Unginčius, H. Uberall, and G. H. Rawitscher, Nuclear size effects in the polaraization of elastically scattered electrons, Nucl. Phys. **A158**, 418 (1970).
[17] X. Roca-Maza, Mott polarimetry at JLAB: Working notes on theory, JLAB Report No. TN-16-019 (2016).
[18] X. Roca-Maza, Theoretical calculations for precision polarimetry based on Mott scattering, Europhys. Rev. Sci. Instrs. Lett. **120**, 33002 (2017).
[19] E. Zeitler and H. Olsen, Screening effects in elastic electron scattering, Phys. Rev. **136**, A1546 (1964).
[20] J. M. Grames, Ph.D. thesis, University of Illinois, 1998.
[21] J. S. Price *et al.*, 5 MeV Mott polarimeter development at Jefferson laboratory, in *Proceedings of the Seventh International Workshop on Polarized Gas Targets and Polarized Beams*, edited by R. J. Holt and M. A. Miller, AIP Conf. Proc. No. 421 (AIP, Woodbury, NY, 1998), p. 446.
[22] M. Steigerwald, MeV Mott polarimetry at Jefferson lab, in *Proceedings of the Fourteenth International Spin Physics Symposium, SPIN2000*, edited by K. Hatanaka *et al.*, AIP Conf. Proc. No. 570 (AIP, Woodbury, NY, 2001), p. 935.
[23] H. Wegener, Mott-streuung an streufolien endlicher dicke, Z. Phys. A **151**, 252 (1958).
[24] V. Tioukine, K Aulenbacher, and E. Riehn, A Mott polarimeter operating at MeV electron beam energies, Rev. Sci. Instr. **82**, 033303 (2011).
[25] J. M. Grames *et al.*, Unique electron polarimeter analyzing power comparison and precision spin-based energy measurement, Phys. Rev. ST: Accel. Beams **7**, 042802 (2004).
[26] X. Roca-Maza *et al.*, Theoretical study of elastic electron scattering off stable and exotic nuclei, Phys. Rev. C **78**, 044332 (2008).
[27] F. Salvat *et al.*, ELSEPA-Dirac partial-wave calculation of elastic scattering of electrons and positrons by atoms, positive ions and molecules, Comp. Phys. Comm. **165**, 157 (2005).
[28] J. Desclaux, A multiconfiguration relativistic DIRAC-FOCK program, Computer Phys. Comm. **9**, 31 (1975).
[29] J. B. Furness and I. E. McCarthy, Semiphenomenological optical model for electron scattering on atoms, J. Phys. B **6**, 2280 (1973).
[30] F. Salvat, Optical-model potential for electron and positron elastic scattering by atoms, Phys. Rev. A **68**, 012708 (2003).
[31] D. H. Jakubassa-Amundsen, The influence of vacuum polarization on the Sherman function during elastic electron-nucleus scattering, arXiv:1407.6809v1.
[32] V. M. Shabaev *et al.*, QED corrections to the radiative recombination of an electron with a bare nucleus, Phys. Rev. A **61**, 052112 (2000).
[33] W. R. Johnson *et al.*, Radiative corrections to the coulomb scattering asymmetry function, Phys. Rev. **126**, 352 (1962).
[34] P. A. Adderley *et al.*, Load-locked dc high voltage GaAs photogun with a inverted ceramic insulator, Phys. Rev. ST: Accel. Beams **13**, 010101 (2010).
[35] T. Maruyama *et al.*, Systematic study of polarized electron emission from strained GaAs/GaAsP superlattice photocathodes, Appl. Phys. Lett. **85**, 2640 (2004).
[36] J. Hansknecht and M. Poelker, Synchronous photoinjection using a frequency-doubled gain-switched fiber-coupled seed laser and ErYb-doped fiber amplifier, Phys. Rev. ST: Accel. Beams **9**, 063501 (2006).
[37] A. Fragemann, V. Pasiskevicius, and F. Laurell, Optical parametric amplification of a gain-switched picosecond laser diode, Opt. Express **13**, 6483 (2005).
[38] J. Grames *et al.*, Two Wien filter spin flipper, in Proceedings of the 2011 Particle Accelerator Conference, 2011 (unpublished), p. 882.
[39] J. Grames, Mott experiment run 1/2 beam energies, JLAB Report No. TN-17-001 (2017).
[40] D. Androic *et al.*, Precision measurement of the weak charge of the proton, Nature (London) **557**, 207 (2018).
[41] J. Grames, Fall 2014 Mott target replacement and ladder position re-calibration, JLAB Report No. TN 14-026 (2014).
[42] R. Sulieman, Mott detectors and data acquisition system, JLAB Report No. TN-17-018 (2017).
[43] https://root.cern.ch/.
[44] G. G. Ohlsen and P. W. Keaton, Techniques for measurement of spin ½ and spin 1 polarization analyzing tensors, Nucl. Instr. Meth. **109**, 41 (1973).
[45] D. Moser, T. Gay, and M. Stutzman, Mott experiment I/II data analysis, JLAB Report No. TN 17-025 (2017).
[46] J. Grames and B. Freeman, Beam systematics for Mott experiment run 1 and 2, JLAB Report No. TN-17-007 (2017).

[47] C. Hovater (private communication).
[48] K. Aulenbacher *et al.*, Precision electron beam polarimetry for next generation nuclear physics experiments, Int. J. Modern Phys. **27**, 1830004 (2018).
[49] G. D. Fletcher, T. J.Gay, and M. S.Lubell, New insights into Mott-scattering electron polarimetry, Phys. Rev. A **34**, 911 (1986).
[50] S. Sirca and M. Horvat, *Computational Methods for Physicists* (Springer, New York, 2012).
[51] P. R. Bevington and D. K. Robinson, Data reduction and error analysis for the physical sciences, in *Data Reduction and Error Analysis* (McGraw-Hill, New York, 2003).
[52] T. J. Gay, J. A. Brand, J. E. Furst, M. A. Khakoo, W. V. Meyer, W. M. K. P. Wijayaratna, and F. B. Dunning, Extrapolation procedures in Mott electron polarimetry, Rev. Sci. Instrum. **63**, 114 (1992).
[53] S. Agostinelli, J. Allison, K. Amako, J. Apostolakis, H. Araujo, P. Arce *et al.*, GEANT4: a simulation toolkit, Nucl. Inst. Meth. A **506**, 250 (2003); J. Allison, K. Amako *et al.*, GEANT4 developments and applications, IEEE Trans. Nucl. Sci. **53**, 270 (2006); J. Allison *et al.*, Recent developments in GEANT4, Nucl. Inst. Meth. A **835**, 186 (2016).
[54] M. H. Kalos and P. A. Whitlock, *Monte Carlos Methods* (Wiley, New York, 2004).
[55] M. Friend *et al.*, Upgraded photon calorimeter with integrating readout for the Hall A Compton polarimeter at Jefferson Lab, Nucl. Instr. Meth. A **676**, 96 (2012).
[56] J. A. Magee *et al.*, A novel comparison of Moller and Compton electron beam polarimeters, Phys. Lett. B **766**, 339 (2017).
[57] A. Narayan *et al.*, Precision Electron-Beam Polarimetry at 1 GeV using Diamond Microstrip Detectors, Phys. Rev. X **6**, 011013 (2016).
[58] A. Rakhman *et al.*, A high-finesse Fabry-Perot cavity with a frequency-doubled green laser for precision Compton polarimetry at Jefferson Lab, Nucl. Instr. Meth A **822**, 82 (2016).
[59] M. Pirbhai *et al.*, A compact inline optical electron polarimeter, Rev. Sci. Instr. **84**, 053113 (2013).
[60] K. Trantham, K. Foreman, and T. Gay, Demonstration of vacuum strain effects on a light-collection lens used in optical polarimetry, Appl. Optics **59**, 2715 (2020).
[61] M. L. Stutzman, Mott target ladder gold foil thickness measurement, JLAB Report No. TN-16-049 (2016).
[62] Available from https://imagej.nih.gov/index.html.